Circadian tumor infiltration and function of CD8+ T cells dictate immunotherapy efficacy

Wang, Chen; Zeng, Qun; Gul, Zeynep Melis; Wang, Sisi; Pick, Robert; Cheng, Phil; Bill, Ruben; Wu, Yan; Naulaerts, Stefan; Barnoud, Coline; Hsueh, Pei-Chun; Moller, Sofie Hedlund; Cenerenti, Mara; Sun, Mengzhu [**and 13 more**]

How to cite

WANG, Chen et al. Circadian tumor infiltration and function of CD8+ T cells dictate immunotherapy efficacy. In: Cell, 2024, vol. 187, n° 11, p. 2690–2702.e17. doi: 10.1016/j.cell.2024.04.015

This publication URL: https://archive-ouverte.unige.ch/unige:177756

Publication DOI: 10.1016/j.cell.2024.04.015

CellPress
OPEN ACCESS

Cell

Article

Circadian tumor infiltration and function of CD8+ T cells dictate immunotherapy efficacy

Chen Wang (王宸),[1,17,*] Qun Zeng (曾群),[1,17] Zeynep Melis Gül,[1] Sisi Wang,[2] Robert Pick,[1] Phil Cheng,[3] Ruben Bill,[1,4,5] Yan Wu,[6] Stefan Naulaerts,[7] Coline Barnoud,[1] Pei-Chun Hsueh,[8,9] Sofie Hedlund Moller,[8,9] Mara Cenerenti,[1] Mengzhu Sun,[1] Ziyang Su,[1] Stéphane Jemelin,[1] Volodymyr Petrenko,[10,11,12,13] Charna Dibner,[10,11,12,13] Stéphanie Hugues,[1,2,14] Camilla Jandus,[1,2,9,14] Zhongwu Li,[6] Olivier Michielin,[2,3] Ping-Chih Ho,[8,9] Abhishek D. Garg,[7] Federico Simonetta,[2,15] Mikaël J. Pittet,[1,2,4,9,14] and Christoph Scheiermann[1,2,13,14,16,18,*]

[1]Department of Pathology and Immunology, Faculty of Medicine, University of Geneva, 1211 Geneva, Switzerland
[2]Translational Research Centre in Onco-Hematology (CRTOH), Geneva 1211, Switzerland
[3]Department of Oncology and Precision Oncology Service, Geneva University Hospitals, University of Geneva, Geneva 1211, Switzerland
[4]AGORA Cancer Research Center, Lausanne 1011, Switzerland
[5]Center for Systems Biology, Massachusetts General Hospital Research Institute and Harvard Medical School, Boston, MA 02114, USA
[6]Key Laboratory of Carcinogenesis and Translational Research, Department of Pathology, Peking University Cancer Hospital & Institute, Beijing 100142, China
[7]Laboratory of Cell Stress & Immunity, Department of Cellular & Molecular Medicine, KU Leuven, Leuven 3000, Belgium
[8]Department of Fundamental Oncology, University of Lausanne, Lausanne 1066, Switzerland
[9]Ludwig Institute for Cancer Research, Lausanne 1005, Switzerland
[10]Division of Thoracic and Endocrine Surgery, Department of Surgery, Geneva University Hospitals, Geneva 1205, Switzerland
[11]Department of Cell Physiology and Metabolism, Faculty of Medicine, University of Geneva, Geneva 1211, Switzerland
[12]Diabetes Center, Faculty of Medicine, University of Geneva, Geneva 1211, Switzerland
[13]Institute of Genetics and Genomics of Geneva (iGE3), Geneva 1211, Switzerland
[14]Geneva Centre for Inflammation Research (GCIR), Geneva 1211, Switzerland
[15]Division of Hematology, Department of Oncology, Geneva University Hospitals, University of Geneva, Geneva, Switzerland
[16]Biomedical Center (BMC), Institute for Cardiovascular Physiology and Pathophysiology, Walter Brendel Center for Experimental Medicine (WBex), Faculty of Medicine, Ludwig-Maximilians-Universität (LMU) Munich, Planegg-Martinsried 82152, Germany
[17]These authors contributed equally
[18]Lead contact
*Correspondence: chen.wang.1@unige.ch (C.W.), christoph.scheiermann@unige.ch (C.S.)
https://doi.org/10.1016/j.cell.2024.04.015

SUMMARY

The quality and quantity of tumor-infiltrating lymphocytes, particularly CD8+ T cells, are important parameters for the control of tumor growth and response to immunotherapy. Here, we show in murine and human cancers that these parameters exhibit circadian oscillations, driven by both the endogenous circadian clock of leukocytes and rhythmic leukocyte infiltration, which depends on the circadian clock of endothelial cells in the tumor microenvironment. To harness these rhythms therapeutically, we demonstrate that efficacy of chimeric antigen receptor T cell therapy and immune checkpoint blockade can be improved by adjusting the time of treatment during the day. Furthermore, time-of-day-dependent T cell signatures in murine tumor models predict overall survival in patients with melanoma and correlate with response to anti-PD-1 therapy. Our data demonstrate the functional significance of circadian dynamics in the tumor microenvironment and suggest the importance of leveraging these features for improving future clinical trial design and patient care.

INTRODUCTION

Immunotherapy is currently one of the most effective means of controlling tumors and, in some cases, curing patients.[1] The most promising interventions involve the injection of chimeric antigen receptor (CAR) T cells or immune checkpoint inhibitors (also known as immune checkpoint blockers [ICBs]).[2,3] CAR T cell therapy consists of administering to the patient T cells that are genetically engineered to recognize tumor cells.[4] ICB therapy aims to activate the antitumor functions of endogenous T cells; for example, the administration of an anti-programmed cell death protein 1 (PD-1) antibody inhibits suppressive molecules on the surface of T cells, thereby activating them.[5]

Anti-tumor immunity has recently been demonstrated to be time-of-day dependent.[6] Specifically, dendritic cells are more effective in controlling tumors grafted into mice at specific times

of the day.[6] Overall functions of the immune system are under a circadian, ~24 h control.[7–13] Leukocytes emigrate from blood to tissues such as lymph nodes in a rhythmic fashion,[14–18] which has been associated with better antigen recognition at specific times of the day.[19–21] In addition to trafficking properties, the phenotype of immune cells is also time-of-day gated, so that stimulation at a specific time of the day yields different outcomes in the associated immune responses.[22,23] This has been linked to time-of-day dependent reactions to vaccines in mice and humans[24,25] and was recently extended also to anti-tumor vaccinations.[6] Although the immune system is highly rhythmic in the steady state and after inflammatory challenge, it is unknown whether circadian rhythms regulate the distribution and phenotype of immune cells within tumors.

Considering that the immune system is under circadian control, it seems important to define the possible relevance of circadian rhythm in an immunotherapy context. Here, we set out to define whether the tumor microenvironment (TME) itself exhibits circadian oscillations. We demonstrate that tumor-infiltrating leukocytes (TILs) exhibit circadian oscillations in both number and phenotype, which can be exploited therapeutically with timed administration of CAR T cells or ICBs.

RESULTS

Leukocyte infiltration of tumors exhibits circadian oscillations

We explored whether the number of leukocytes in tumors exhibits time-of-day differences, by injecting B16-F10 melanoma cells expressing ovalbumin (B16-F10-OVA) subcutaneously (s.c.) into cohorts of mice at one time of the day (that is, at zeitgeber time 9 [ZT9; 9 h after light onset in a 12 h light/12 h dark environment]) and harvested tumors 12 days later at 4 different times of the day (ZT1 [“morning”], ZT7 [“day”], ZT13 [“evening”], and ZT19 [“night”]). The overall number of TILs was highly dependent on the time of day of tumor harvest, with total leukocyte numbers peaking in the evening (ZT13) (Figures 1A and S1A). Specifically, we detected time-of-day differences in the numbers of tumor $CD4^+$ and $CD8^+$ T cells, $NK1.1^+$ cells, $CD11b^+Ly6C^+$ cells, $CD11c^+MHCII^+$ as well as $CD19^+$ cells (phase-shifted from blood leukocyte counts), whereas $CD11b^+F4/80^+$ cells and $CD11b^+Ly6G^+$ cells did not exhibit significant changes (Figures 1A, S1B, and S1C). We confirmed these data by immunofluorescence staining of tumor sections, showing higher T cell numbers in the evening (ZT13) compared with the morning (ZT1) (Figure 1B). We did not observe significant differences in tumor volume within a day (Figure S1D), and although tumors had longer times to grow when harvested at night (ZT19) compared with the evening (ZT13), we observed higher leukocyte numbers in the evening (Figure 1A). This demonstrated that differences in leukocyte numbers were due to the time of day of tumor harvest. We further observed no changes in vascular density in the tumor (Figure S1E), indicating this phenotype to be immune cell specific. We confirmed the phenotype in a spontaneous melanoma tumor model (*Tyr::Cre^{ERT2}; Pten^{loxP}; BRaf^{CA}*)[26] (Figures 1C, S1A, and S1F), which together demonstrated that numbers of TILs exhibit time-of-day differences, peaking in the evening.

We next transferred animals to complete darkness conditions, as circadian rhythms persist even under constant environmental conditions, such as in the absence of rhythmic lighting patterns. Constant darkness did not alter the observed time-of-day differences, demonstrating these oscillations to be bona fide circadian in nature and not simply a response to a rhythmic light:dark environment (Figure 1D). However, switching mice from a normal light-dark to a 12 h inverted dark-light cycle inversed TIL numbers (Figures 1E and 1F). This demonstrated that the oscillations were not dependent on light per se but that they could be synchronized to a new lighting regime. This ability to be synchronized by an external cue is an additional feature of circadian rhythms (Figure 1F). Subjecting mice to an acute jet-lag protocol, which consisted of shifting mice to a 6 h phase-delay and harvesting tissues at the previously assessed respective morning and evening time points thereafter (Figure 1E), furthermore abrogated time-of-day differences in TILs (Figure 1F). Together, these data provide unexpected evidence that TILs exhibit circadian oscillations in cellularity, a process that is entrained by light.

Endothelial cells gate circadian leukocyte infiltration

To assess the etiology of these oscillations, we quantified whether leukocyte proliferation, death, egress, and/or infiltration exhibited time-of-day differences. We did not observe significant differences in total leukocyte proliferation, apoptosis, or egress (Figures S2A–S2C). By contrast, an acute (24 h) block of leukocyte infiltration with an anti-lymphocyte function-associated antigen 1 (LFA-1)-integrin (anti-$\alpha_L\beta_2$) antibody greatly reduced leukocyte counts in the tumor in the evening (ZT13) and abrogated the time-of-day differences (Figure 2A). This suggested that leukocyte input from the blood accounted for the time-of-day differences and was required to maintain overall TIL cellularity. It further indicated that leukocyte supply to the tumor from the blood was surprisingly dynamic over such a short time frame. Leukocyte infiltration into the tumor from blood was of functional relevance since chronic anti-LFA-1-integrin treatment strongly increased tumor volume (Figure S2D). To investigate whether leukocytes indeed infiltrated the tumor in a time-of-day-dependent manner, we performed short-term (2 h) homing assays with adoptively transferred leukocytes. Cells were harvested from donor mice at one time of the day and intravenously (i.v.) injected into phase-shifted recipients, housed in cabinets with inverted lighting regimes, thus limiting the variable to timing in the recipient only. Leukocyte trafficking to the tumor was strongly time-of-day dependent, with more cells reaching the tumor in the evening, in line with the infiltration block data (Figure 2B). This demonstrated that, in mice, the TME exhibited pro-migratory properties in the evening, which were not driven by differences in vascular density (Figure S1E). Since the $\alpha_L\beta_2$-integrin mediated leukocyte infiltration (Figure 2A), we quantified expression levels of its ligands on endothelial cells of the tumor vasculature, as gatekeepers located at the blood-tumor interphase. Intercellular adhesion molecule 1 (ICAM-1) was much higher expressed by endothelial cells in the evening (ZT13) compared with the morning (ZT1) (Figure 2C), whereas vascular cell adhesion molecule 1 (VCAM-1) as well as E-selectin, additional endothelial cell adhesion molecules, did not exhibit time-of-day differences (Figure S2E). This phenotype was still present

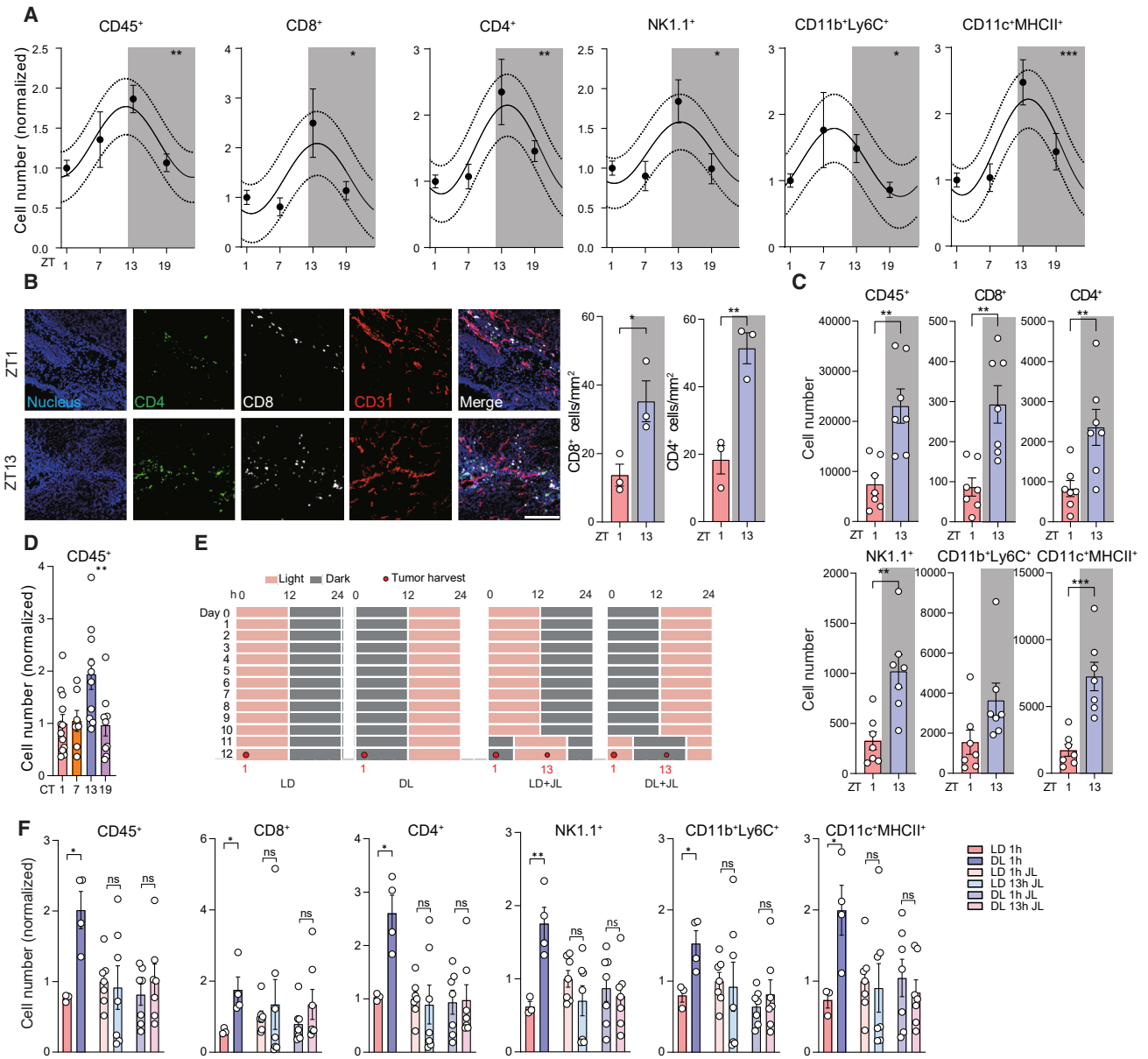

Figure 1. Time of day of harvest dictates numbers of tumor-infiltrating leukocytes

(A) Normalized total numbers of tumor-infiltrating leukocytes in a B16-F10-OVA tumor, harvested at 4 different times of the day (zeitgeber time [ZT]); $n = 15, 11, 11, 12$ mice from 4 independent experiments, cosinor analysis. Shaded areas indicate dark phases.

(B) Imaging (left) and quantification (right) of $CD4^+$ and $CD8^+$ T cells in B16-F10-OVA tumors harvested at ZT1 or ZT13; $n = 3$ mice, unpaired Student's t test, scale bars: 200 μm.

(C) Numbers of tumor-infiltrating leukocytes in *Tyr::CreERT2*, $BRaf^{CA}$, $Pten^{loxP}$ mice harvested at ZT1 or ZT13; $n = 7$ mice, unpaired Student's t test.

(D) Normalized total numbers of tumor-infiltrating leukocytes in a B16-F10-OVA tumor, harvested at different times of the day under constant darkness conditions (circadian time [CT]); $n = 12, 7, 10, 9$ mice, from 3 independent experiments, one-way ANOVA.

(E) Light schedule of light:dark (LD), inverted dark:light (DL), and jet lag (JL) conditions. Shaded areas indicate dark phases, and numbers indicate the harvest times.

(F) Numbers of tumor-infiltrating leukocytes in a B16-F10-OVA tumor, harvested as the indicated time points (1 or 13 h in E) after the onset of the cycle under light:dark (LD, $n = 3$ mice), inverted dark:light (DL, $n = 4$ mice), or corresponding jet lag (JL, $n = 7$ mice) conditions, from 3 independent experiments, unpaired Student's t test. Shaded areas indicate dark phases. All data are represented as mean ± SEM, ns, not significant, $^*p < 0.05$; $^{**}p < 0.01$; $^{***}p < 0.001$. See also Figure S1.

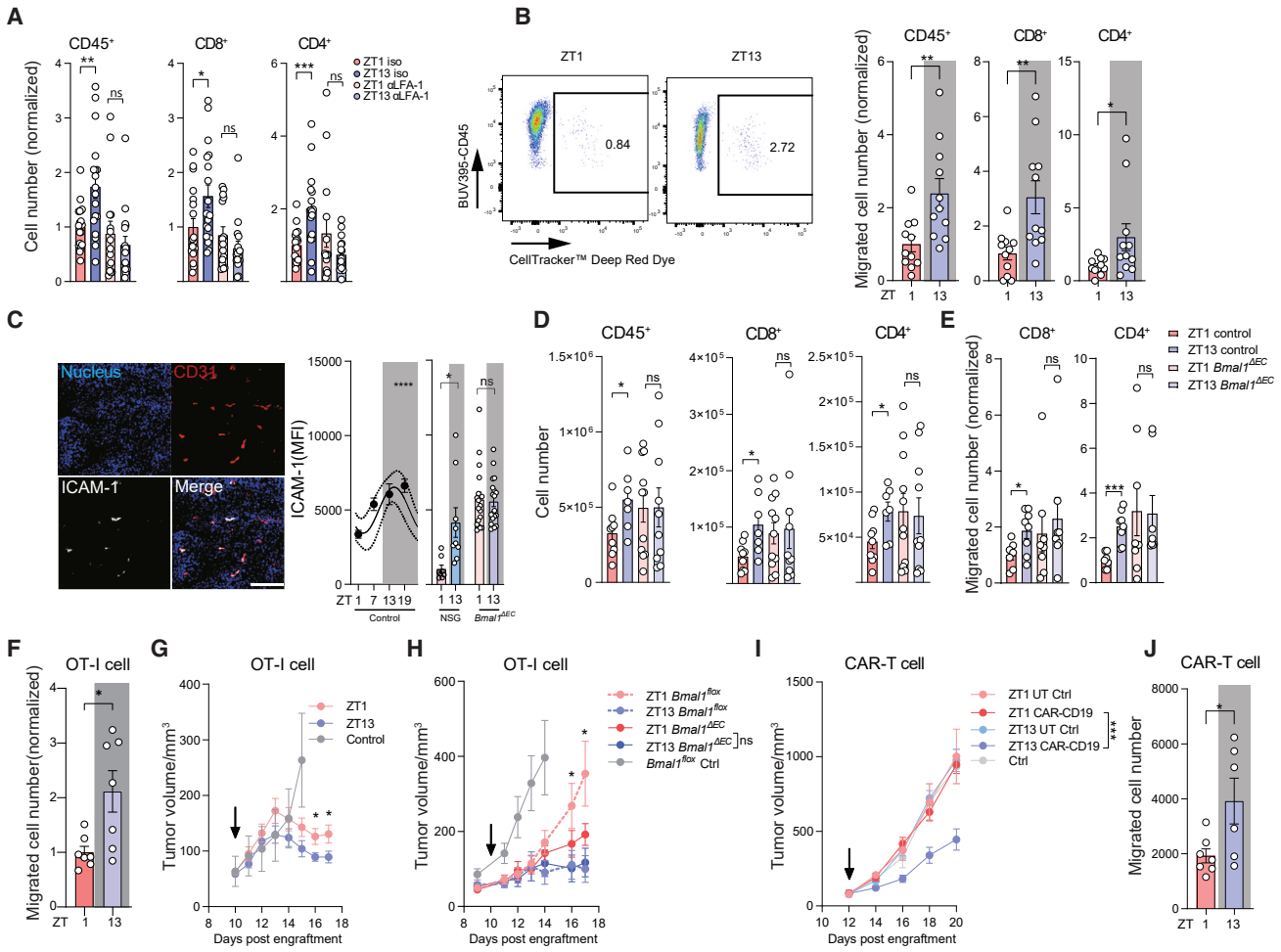

Figure 2. Endothelial cells gate circadian leukocyte infiltration and T cell therapy

(A) Normalized total numbers of tumor-infiltrating leukocytes in a B16-F10-OVA model, harvested at ZT1 or ZT13, 24 h after the treatment of isotype control or anti-LFA-1 antibodies; n = 19, 18, 15, 16 mice, from 5 independent experiments, unpaired Student's t test.

(B) Gating strategy and quantification of adoptively transferred cells in B16-F10-OVA tumors 2 h post i.v. injection at ZT1 or ZT13; n = 11 mice, from 2 independent experiments, unpaired Student's t test.

(C) Imaging (left) and quantification (right) of ICAM-1 expression on CD31$^+$ endothelial cells in B16-F10-OVA tumors, harvested at ZT1 or ZT13 from control (pooled of B6 mice and *Bmal1*^{flox} mice), NSG or *Bmal1*$^{\Delta EC}$ mice; n = 50, 12, 47, 15, 8, 9, 18, 19 sections, from 16, 4, 15, 5, 3, 3, 5, 5 mice, respectively, from 4 independent experiments, unpaired Student's t test and cosinor analysis, scale bars: 200 μm.

(D) Numbers of leukocytes in B16-F10-OVA tumors, harvested at ZT1 or ZT13 from littermate control or *Bmal1*$^{\Delta EC}$ mice; n = 9, 7, 11, 10 mice, from 4 independent experiments, unpaired Student's t test.

(E) Normalized numbers of adoptively transferred leukocytes harvested from B16-F10-OVA tumors 2 h post i.v. injection at ZT1 or ZT13 into littermate control or *Bmal1*$^{\Delta EC}$ mice; n = 7, 8, 8, 8 mice, from 2 independent experiments, unpaired Student's t test.

(F) Normalized numbers of adoptively transferred OT-I cells in B16-F10-OVA tumors 2 h post injection at ZT1 or ZT13; n = 7 mice, from 2 independent experiments, unpaired Student's t test.

(G) Tumor volume after i.v. injection of 10^6 activated OT-I cells at ZT1 (n = 14 mice) or ZT13 (n = 13 mice), control (n = 11 mice), from 3 independent experiments, Student's t test.

(H) Tumor volume after i.v. injection of 10^6 activated OT-I cells at ZT1 (*Bmal1*^{flox}, n = 5 mice, *Bmal1*$^{\Delta EC}$, n = 6 mice) or ZT13 (n = 6 mice), control (n = 8 mice), from 2 independent experiments, Student's t test, ***Bmal1*^{flox} ZT1 vs. ZT13.

(I) Tumor volume after i.v. injection of 10^6 human CD19 CAR-CD28-CD3ζ T cells in DoHH2 tumor-bearing NSG mice at ZT1 (UT, untransduced T cells, n = 5 mice, CAR T, n = 7 mice) or ZT13 (UT, n = 5 mice, CAR T, n = 7 mice), control (n = 4 mice), from 2 independent experiments, two-way ANOVA.

(J) Number of CAR T cells in DoHH2 tumors 24 h post i.v. injection at ZT1 (n = 7 mice) or ZT13 (n = 6 mice), from 2 independent experiments, unpaired Student's t test. All data are represented as mean ± SEM, ns, not significant, *p < 0.05; **p < 0.01; ***p < 0.001; ****p < 0.0001. See also Figure S2.

in highly immune-deficient NOD *scid* gamma (NSG) mice, indicating that these differences were not caused by the observed oscillations in the tumor leukocyte infiltrate (Figure 2C). We thus focused on endothelial cells as potential mediators of circadian leukocyte infiltration and grafted tumors into animals exhibiting an inducible, lineage-specific lack of the circadian gene

BMAL1 in endothelial cells (*Cdh5*^{creERT2}:*Bmal1*^{flox}, *Bmal1*$^{\Delta EC}$). In *Bmal1*$^{\Delta EC}$ mice, time-of-day differences in ICAM-1 expression in tumor endothelial cells were completely abrogated (Figure 2C), yet vascular density was similar to wild-type mice (Figure S1E). Furthermore, total tumor leukocyte numbers in *Bmal1*$^{\Delta EC}$ mice (Figure 2D) as well as adoptively transferred leukocyte infiltration to the tumor ceased to be time-of-day dependent (Figure 2E). Together, these data demonstrate that endothelial cells control a rhythmic leukocyte infiltration process into tumors, which peaks in the evening and is dependent on the endothelial cell-autonomous circadian clock machinery.

Efficacy of CAR T cell therapy is time-of-day dependent

Given that T cells currently represent the most promising target of anti-cancer immunotherapies,[27] we focused our subsequent functional assays on these cells. To evaluate a potential clinical translational aspect of rhythmic T cell infiltration into tumors, we initially harvested OVA-specific CD8$^+$ T cells from OT-I mice and performed T cell therapy on mice engrafted with B16-F10-OVA-expressing tumors. After i.v. adoptive transfer of activated OT-I cells into tumor-bearing mice 10 days after tumor engraftment, we detected significantly increased numbers of transferred cells, when T cell infusion had been administered at ZT13 compared with ZT1 (Figure 2F). Of relevance, this yielded significantly better tumor control and reduced tumor burden (Figures 2G and S2F). By contrast, in *Bmal1*$^{\Delta EC}$ mice, the time-of-day effects were abrogated, demonstrating that the therapeutic benefit was governed by the endothelial cell-autonomous circadian clock (Figures 2H and S2G). To further evaluate a potential clinical translational aspect of rhythmic T cell infiltration into tumors, we employed human CAR T cells, bearing an anti-human CD19 CAR (CD19 CAR-CD28-CD3ζ). NSG mice were engrafted with DoHH2 cells, a tumor cell line for human diffuse large B cell lymphoma (DLBCL), the major indication for CAR T cell therapy in the clinic.[28,29] Tumor-bearing mice were treated with CAR T cells in a time-of-day-dependent manner, with infusion of CAR T cells at ZT13 showing a reduction in tumor volume, while infusion at ZT1 had no effect on tumor control (Figures 2I and S2H). This observation was linked to increased CAR T cell homing after 24 h at ZT13 compared with ZT1 in these animals (Figure 2J), in line with our previous observation (Figure 2B). These data demonstrate clearly enhanced T cell therapy efficacy, simply by adjusting the time of injection to the optimal leukocyte infiltration time of the day.

Diurnal differences in TIL phenotype

Knowing that the number of TILs depends on the time of day and that this variable could be exploited for therapeutic purposes, we next assessed whether the phenotype of TILs was also time-of-day dependent. To this end, we performed single-cell RNA sequencing (scRNA-seq) analyses of the CD45$^+$ population, sorted from tumors 12 days after engraftment and harvested at four different times of the day, at ZT1, ZT7, ZT13, and ZT19, analogous to the previous experiments. Uniform manifold approximation and projection (UMAP) analyses revealed 18 distinct leukocyte populations, providing insights into subsets and states of leukocytes (Figures S3A–S3C, S4A, and S4B). The most prominent population consisted of macrophages, which made up 17%–28% of the infiltrate, followed by natural killer (NK) cells (10%–22%) and B cells (5%–18%) (Figures S4A and S4B). Circadian clock genes were expressed rhythmically in all leukocyte subsets with *Per1* exhibiting the most wide-spread oscillation, peaking at ~ZT13 (Figures 3A and S4C). Macrophages displayed the highest number of oscillating genes, followed by monocytes and NK cells (Figure S4D). However, each immune cell population exhibited distinct oscillatory gene signatures (Figures S4D–S4F; Table S1). Gene ontology analyses showed that oscillating genes were mostly enriched in metabolism but also showed differences in cell adhesion and differentiation as well as T cell activation (Figure S4E; Table S1). These data indicate that the number and phenotype of immune cells in the TME are highly oscillatory and strongly depend on the time of day.

Time-of-day differences in the tumor T cell phenotype

Focusing on T lymphocytes, we performed further analyses and detected 15 subclusters, with CD8$^+$ T cells representing the largest population (Figures 3B, 3C, and S5A–S5C). We observed significant time-of-day-dependent changes in the ratio of cell clusters defined as "anti-" versus "pro-tumorigenic" lymphocytes (see STAR Methods for cluster definition), peaking at ZT13 and troughing at ZT1 (Figure 3D). Furthermore, the ratio in clusters defined as "non-exhausted" versus "exhausted" CD8$^+$ T cells exhibited differences, a phenotype we also observed by flow cytometry (Figures 3E and S5D), which could be further refined to the ratio of CD8$^+$ T cells defined as "effector memory" versus exhausted (Figure 3D). This suggested that CD8$^+$ T cells exhibited a more suppressed phenotype in the morning and a more anti-tumorigenic signature in the evening. To investigate this, we defined the gene signatures of T cells expressed in the evening (ZT13) versus the morning (ZT1) (Table S2). The evening signature was enriched in leukocyte adhesion and T cell activation pathways (Figure 3F) and was indeed strongly correlated with better survival in human melanoma patients from the The Cancer Genome Atlas (TCGA) dataset, indicating higher anti-tumorigenic immunogenicity of this gene expression signature (Figure 3G). These data show that in addition to oscillations in the number of T cells in the TME, their function also changes in a time-of-day-dependent manner.

CD8$^+$ T cell phenotype oscillates

These expression data indicated that T cell function within the TME exhibited time-of-day differences. Genes associated with T cell activation, suppression, migration, and effector functions showed an oscillation in effector CD8 T cells across the day (Figure 4A). Notably, expression of the immune checkpoint gene *Pdcd1* (encoding for PD-1) was rhythmic in this CD8 T cell cluster, peaking at ZT1 and exhibiting a trough at ZT13 (Figures 4A and 4B). This was in line with expression of *Pdcd1* in the whole CD8 T cell population, as assessed by qPCR analyses of sorted CD8 T cells from tumors as well as by pseudobulk analyses of the scRNA-seq data (Figures 4C and S5E). PD-1 was also differently expressed at the cell surface protein level, in line with the transcriptomic analyses, yet phase-shifted, similar to what has been described for other circadian-expressed mRNA-protein pairs[30] (Figure 4D). This difference in PD-1 expression could be abrogated when the clock gene *Bmal1* was deleted in

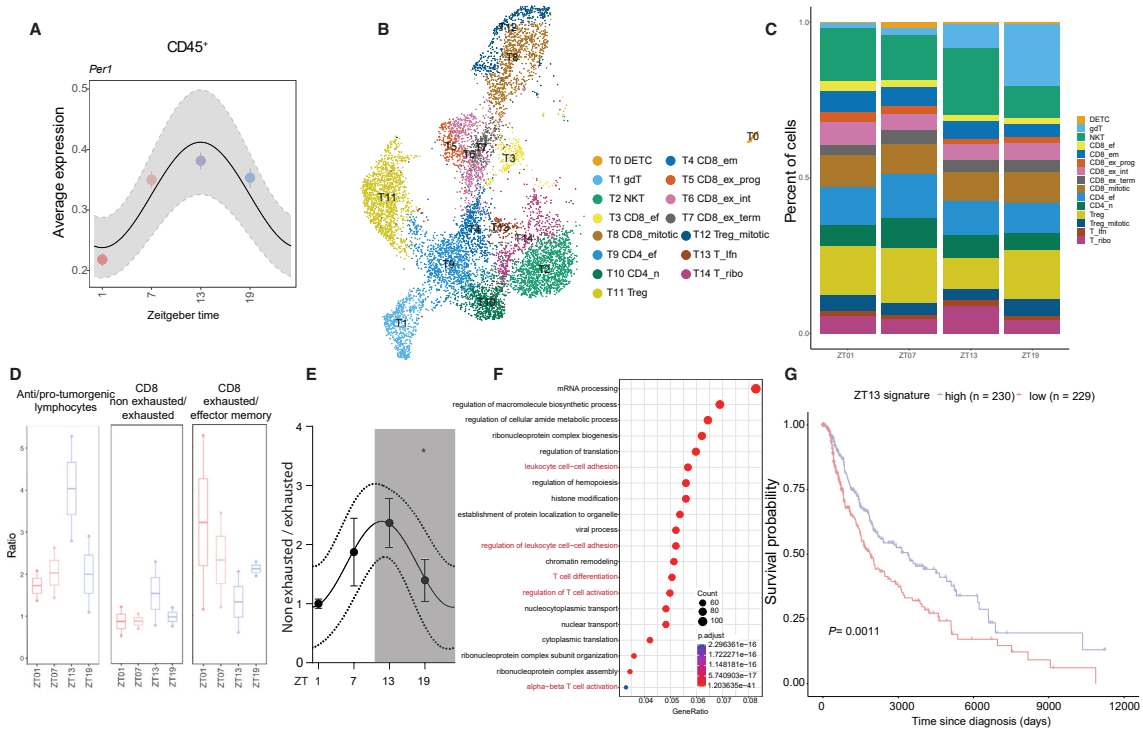

Figure 3. Diurnal differences in T cell parameters

(A) Circadian gene *Per1* expression in total tumor infiltrating leukocyte clusters with fitted cosinor curve (line) and 95% confidence interval (shaded area).

(B) UMAP representation of scRNA-seq analyses of T cells harvested at 4 different times of the day.

(C) Relative abundance of T cell subsets across different times of the day.

(D) Abundance ratio of specific T cell subsets across different times of the day by scRNA-seq. "Anti-tumorigenic lymphocytes" include NK, γδT, natural killer T (NKT), CD8 effector, CD4 naive, CD8 effector memory, CD8 mitotic, and CD4 effector clusters, whereas "pro-tumorigenic lymphocytes" include Treg, Treg mitotic, and CD8 exhausted clusters.

(E) Normalized ratio of non-exhausted over exhausted $CD8^+$ T cells across different times of the day by flow cytometry; n = 14, 8, 20, 8 mice, from 5 independent experiments, cosinor analysis.

(F) Gene ontology analysis of genes oscillating in $CD8^+$ T cells.

(G) Survival analysis in melanoma patients from the TCGA dataset using a high or low expression of the murine ZT13 gene signature in Table S2, logrank test. All data are represented as mean ± SEM, $*p < 0.05$. See also Figures S3–S5 and Table S1.

T cells (*Cd4cre:Bmal1^{flox}, Bmal1$^{\Delta T}$*) (Figure 4E), indicating that rhythmic expression of PD-1 in $CD8^+$ T cells was circadian and cell-intrinsic. To confirm this, we activated $CD8^+$ T cells *in vitro* and synchronized the cells (Figures 4F and S6A). Activated $CD8^+$ T cells showed a strong oscillatory expression of *Pdcd1* after synchronization, which was significantly dampened in T cells harvested from *Bmal1$^{\Delta T}$* mice and *Per1$^{-/-}$Per2$^{-/-}$* animals (Figure 4G). *PDCD1* also exhibited circadian oscillations *in vitro* in synchronized human $CD8^+$ T cells, indicating these oscillations to be of relevance in the human setting as well (Figure 4H). These data demonstrated *Pdcd1* expression in $CD8^+$ T cells to be bona fide circadian and cell autonomous in nature, at both the mRNA and surface protein levels, which might be targetable by anti-PD-1 immune check inhibitors in a time-of-day-dependent manner.

Anti-PD-1 therapy is time-of-day dependent

We therefore assessed the relevance of time-of-day-dependent expression of PD-1 by performing timed administration of anti-PD-1 antibodies. Time of day of antibody administration had a strong impact on tumor growth in the B16-F10-OVA melanoma tumor model, with tumors growing less when therapy was performed in the evening compared with the morning (Figures 5A, 5B, and S6B). In fact, therapy in the morning had surprisingly little effect on tumor burden, even when morning administration preceded that of evening administration by 12 h (Figures 5A, 5B, and S6B). We could confirm these data in an MC-38 colon carcinoma model, indicating that this phenotype extended to other tumor models (Figures S6C and S6D). The time-of-day effect was critically dependent on $CD8^+$ T cells, as anti-PD-1 therapy yielded no benefit in a scenario where $CD8^+$ T cells had previously been depleted (Figures 5C and S6E). Furthermore, the T cell circadian clock machinery was required since circadian oscillations were altered in *Bmal1$^{\Delta T}$* mice, demonstrating the T cell clock to be mediating the phenotype (Figures 5D, S6F, and S6G). Using several cycles of timed anti-PD-1 therapy and combinations of evening and morning administrations, we observed that time of day of the first treatment was responsible for the difference, in contrast to the subsequent dose (Figures 5E and S6H). We thus focused on the first administration cycle to further elucidate the underlying mechanism and performed flow

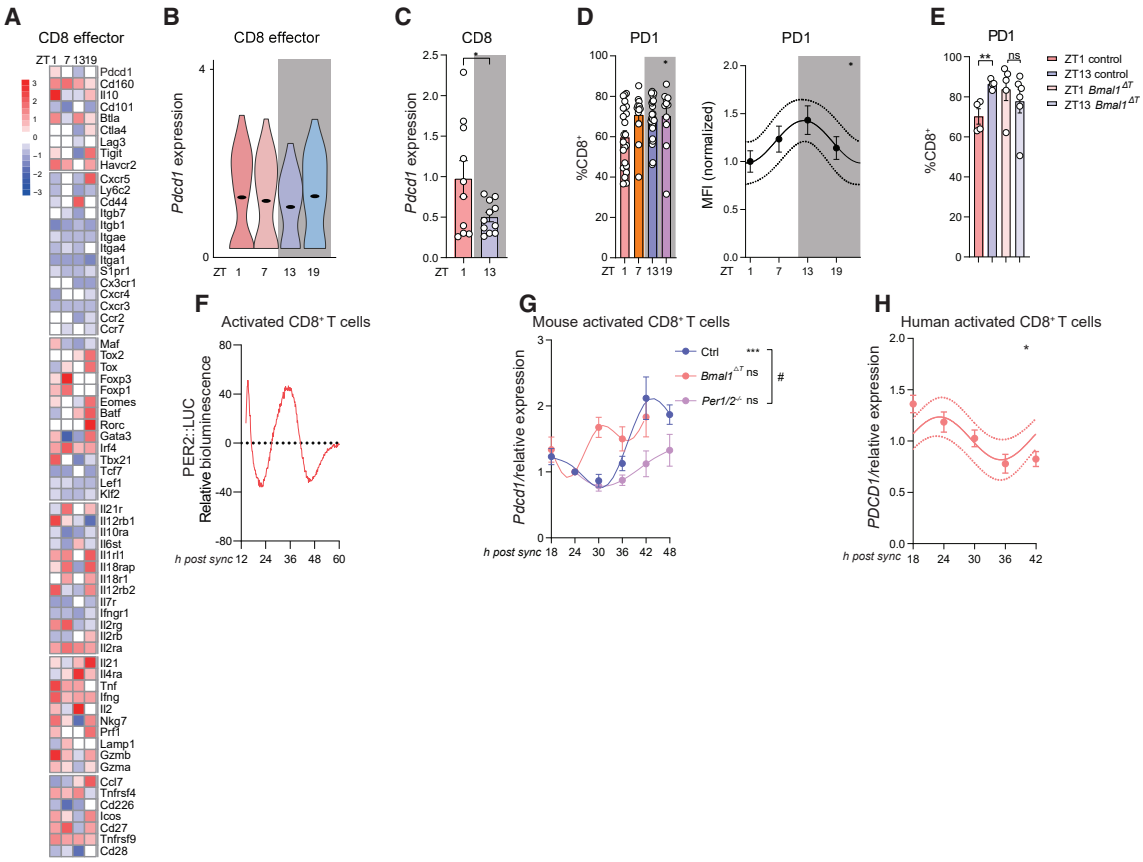

Figure 4. CD8$^+$ T cell phenotype oscillates

(A) Heatmap of scRNA-seq analyses of CD8$^+$ effector T cells, harvested at 4 different times of the day.

(B) *Pdcd1* expression by scRNA-seq of CD8$^+$ effector T cells at different times of the day.

(C) *Pdcd1* expression by qPCR of fluorescence-activated cell sorting (FACS)-sorted CD8$^+$ cells from B16-F10-OVA tumors at ZT1 (n = 10 mice) or ZT13 (n = 11 mice), from 3 independent experiments, unpaired Student's t test.

(D) PD-1 expression by flow cytometry of tumor CD8$^+$ T cells harvested at different time (n = 22, 13, 22, 11 mice), from 5 independent experiments, one-way ANOVA and cosinor analysis.

(E) PD-1 expression by flow cytometry of tumor CD8$^+$ T cells, harvested at ZT1 or ZT13 from littermate control (n = 4 mice) or *Bmal1*$^{\Delta T}$ mice (n = 5, 6 mice), unpaired Student's t test.

(F) Relative bioluminescence of activated CD8$^+$ T cells generated from PER2::LUC mice post synchronization, representative data from n = 3 mice.

(G) *Pdcd1* expression of activated CD8$^+$ T cells post synchronization from control (n = 7, 14, 12, 11, 11, 4 mice) or *Bmal1*$^{\Delta T}$ mice (n = 6 mice) or *Per1*$^{-/-}$*Per2*$^{-/-}$ mice (n = 4 mice) from 4 independent experiments, ***cosinor analysis. $^{\#}$Two-way ANOVA.

(H) *PDCD1* expression in human activated CD8$^+$ T cells post synchronization, n = 6, from 4 independent experiments, cosinor analysis. All data are represented as mean ± SEM, *$p < 0.05$; **$p < 0.01$; ***$p < 0.001$. See also Figure S6.

cytometry analyses of CD8$^+$ T cells in the tumor, 24 h after anti-PD-1 treatment performed in the morning compared with the evening. The results indicated that the administration of anti-PD-1 at ZT13 but not at ZT1 caused a significant increase of CD8$^+$ T cell activation and degranulation in the tumor, as shown by higher expression CD137 and CD107a levels, respectively (Figure 5F). Additionally, anti-PD-1 treatment at ZT13 also increased the production of interferon (IFN)γ and Granzyme B in tumor-infiltrating CD8$^+$ T cells compared with ZT1 (Figure 5G). To maximize the observed chrono-therapeutic anti-tumor effects, we combined timed OT-I T cell therapy with timed anti-PD-1 infusion. Activated OT-I T cells were co-injected with anti-PD-1 antibody into phase-shifted mice at ZT13 or at ZT1. Anti-tumor effects were now enhanced, with ZT13 treatment further reducing tumor burden compared with ZT1 conditions (Figures 5H and S6I). This indicates that both CD8$^+$ T cell numbers and phenotype dictate circadian differences in the response to tumor immunotherapy. Together, our data demonstrate a strong time-of-day-dependent phenotype of the tumor immune cell infiltrate, which can be harnessed with timed administration of immunotherapies to maximize anti-tumor effects.

Circadian immune cell phenotype in human cancers

To interrogate whether time-of-day oscillations in the immune cell infiltrate also exist in human tumors, we analyzed human melanoma samples from patients that had undergone surgical removal of the tumor at different times of the day. Using immunohistochemical analyses, we found that numbers of CD4$^+$ and

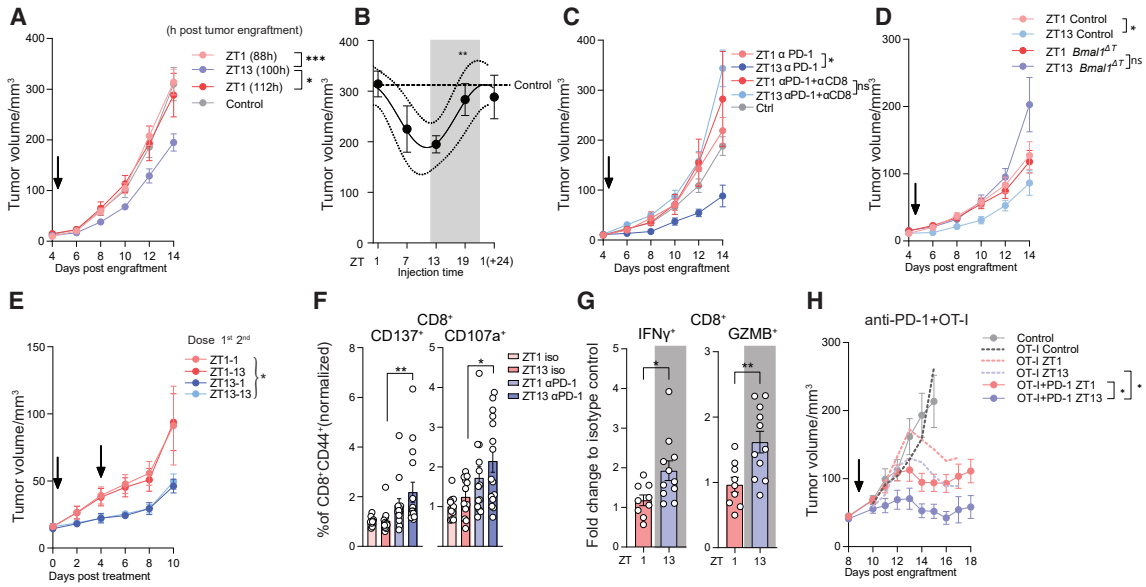

Figure 5. Circadian efficacy of anti-PD-1 treatment

(A) Tumor volume after anti-PD-1 treatment (arrows) administered at ZT1 or ZT13, anti-PD-1 (n = 15, 15, 9 mice), control (n = 11 mice), from 3 independent experiments, two-way ANOVA.

(B) Tumor volume 14 days post tumor engraftment, anti-PD-1 (n = 15, 5, 15, 6, 9 mice), control (n = 11 mice), from 3 independent experiments, cosinor analysis.

(C) Tumor volume after anti-PD-1 treatment (arrows) administered at ZT1 or ZT13 with or without (n = 4 mice) CD8 depletion.

(D) Tumor volume after anti-PD-1 treatment (arrows) administered at ZT1 or ZT13 in control (ZT1, n = 9 mice, ZT13, n = 10 mice) or in *Bmal1*$^{\Delta T}$ (ZT1, n = 9 mice, ZT13, n = 10 mice), from 3 independent experiments, two-way ANOVA.

(E) Tumor volume after two doses of anti-PD-1 treatment (arrows) administered at ZT1 or ZT13; n = 7 mice, from 2 independent experiments, two-way ANOVA.

(F) Phenotype of tumor CD8$^+$ T cell harvested at ZT1 or ZT13, 24 h post isotype control (n = 12 mice) or anti-PD-1 treatment (ZT1, n = 13 mice, ZT13, n = 15 mice), from 4 independent experiments, two-way ANOVA, and Sidak's post test.

(G) Cytokine production by tumor CD8$^+$ T cells harvested at ZT1 (n = 9 mice) or ZT13 (n = 11 mice) 24 h post anti-PD-1 treatment, from 4 independent experiments, unpaired Student's t test.

(H) Tumor volume after control (n = 12 mice) or combination therapy of anti-PD-1 and OT-I cell administration (arrow), administered at ZT1 (n = 6 mice) or ZT13 (n = 5 mice), from 2 independent experiments, two-way ANOVA. Dotted lines indicate tumor growth from Figure 2F. All data are represented as mean ± SEM, ns, not significant, *p < 0.05; **p < 0.01; ***p < 0.001. See also Figure S6.

CD8$^+$ cells exhibited a striking time-of-day-dependent profile with a peak in the early afternoon (Figures 6A and 6B). This indicated that the time of day also dictated numbers of TILs in humans. To obtain broader information with respect to the timed immune cell infiltrate in human tumors, we utilized our mouse scRNA-seq datasets together with publicly available, time-stamped mouse skin scRNA-seq and bulk RNA-seq datasets to train a machine learning model to be able to time stamp sequencing datasets where information on the time of day was not available (Figure 6C). We trained a ZeitZeiger algorithm,[31] using either all genes or conserved coefficients (57 genes), which were predicted by ZeitZeiger to oscillate (Figure 6C; Table S3). Both approaches predicted the time of testing data well—including healthy skin as well as melanoma samples—with an average error of ~1.5 h (Figures S6J–S6L; Table S3). We further validated the ZeitZeiger model on public mouse skin RNA-seq and microarray datasets and again achieved good time stamping (Figures 6D and S6M). This allowed us to correctly identify the time of day of healthy tissues in mice as well as our mouse tumor samples in a blinded manner with an error of ~2 h. Using the trained ZeitZeiger model, we next aimed to predict the time of day of harvest also in human biopsies. Indeed, using publicly available microarray data from healthy human skin where time of day information was known, we could adequately predict the time of day in these samples with an error of <4 h (Figures 6E and S6N). Knowing that the algorithm adequately assigned time of day to human samples, we next assigned time-of-day information to 103 primary melanoma samples from the TCGA dataset. Interestingly, we observed time-of-day differences in the ratio of exhausted CD8$^+$ T cells versus non-exhausted CD8$^+$ T cells, analogous to the mouse data, but—as expected—phase-shifted due to inverted immune oscillations between diurnal humans and nocturnal mice,[14,32] with a higher anti-tumor ratio in the morning compared with the afternoon (Figure 6F). These data indicate that both leukocyte numbers and phenotype in human TILs are time-of-day dependent.

Lastly, we investigated whether the evening RNA signature identified in mouse melanoma T cells was sufficient to correlate with the response of patients to ICBs. Indeed, the signature unveiled a significant difference in the response rate of patients,[33,34] with patients that exhibited a higher expression of this signature in T cells also showing favorable response to ICB treatment (Figure 6G; Table S2). Together, our data provide compelling evidence that the immune cell compartment of

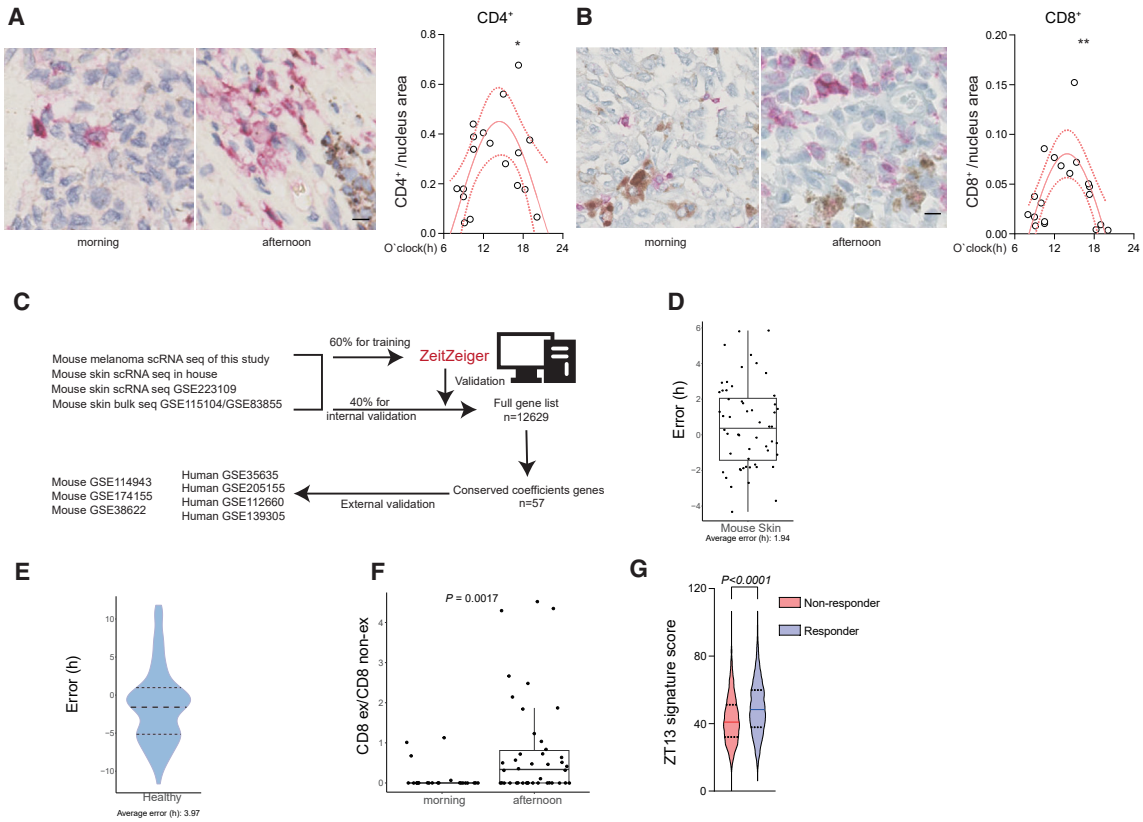

Figure 6. Circadian immune cell phenotype in human cancers

(A and B) Imaging (left) and quantification (right) of CD4$^+$ (n = 18 patients) and CD8$^+$ (n = 19 patients) T cells in human melanoma, harvested at different times of the day, cosinor analysis, scale bar: 10μm, CD8 or CD4 staining in red.

(C) Schematic for the algorithm training and validation to predict time of day in non-time stamped samples. A final algorithm containing 57 genes was used for external validation and prediction.

(D and E) Error (hours) of the time prediction algorithm in external validation in mouse (n = 56 mice) (D) and human (n = 369 samples) (E) tissues.

(F) Exhausted/non-exhausted CD8$^+$ T cell ratio in primary melanoma tissues from the TCGA melanoma dataset, plotted by using the algorithm to predict time of biopsies, morning, n = 24 patients; afternoon, n = 42 patients, Student's t test.

(G) Enrichment of the murine ZT13-gene expression signature in patients responding or not responding to ICB treatment (non-responders, n = 8,608 cells; responders, n = 4,242 cells). All data are represented as median and quartile. See also Figure S6 and Tables S2 and S3.

melanomas is surprisingly time-of-day dependent and that this can be harnessed therapeutically with timed interventions of CAR T cell infusions or immune checkpoint blockade.

DISCUSSION

Here, we provide evidence for circadian dynamics in the tumor immune microenvironment, with functional implications for the optimal time point for the administration of immunotherapies. In patients with melanoma,[35–37] non-small cell lung cancer (NSCLC) patients,[38,39] and patients with metastatic squamous cell carcinoma of the esophagus,[40] retrospective data of matched cohorts treated with ICB was recently indicated to be time-of-day sensitive, with better survival observed after ICB infusion in the morning compared with the afternoon.[35,38,41] These clinical observations are in line with what we define here in mechanistic detail. Future randomized and prospective clinical trials will be required to support that claim.

A key question in the field is the mechanism of these time-of-day effects. Antibody titers remain high over weeks in patients,[42] which may indicate that the observed long-term circadian effects are mediated via the timing of the first interventions. Our data indicate that the first cycle of therapy yields different circadian outcomes and that the timing of the subsequent dose(s) may not be as relevant. Data from retrospective clinical trials support the potential importance of the timing of the first infusion(s) for therapeutic benefits.[36,43] Our data suggest that an antibody infused at different times of the day encounters differences in both the number of immune cells present in the tumor as well as their levels of PD-1. This would mean that the product of circadian changes in numbers and the phenotype of TILs—and thus the target of the antibody—exhibits circadian oscillations, which could be responsible for this chronotherapeutic impact. However, whether local levels of antibody oscillate, such as found within the tumor interstitium, is not known. Tumor macrophages have been shown to quickly strip antibodies off adjacent T cells,[44] which may be an additional mechanism for

time-of-day sensitivity, given that we also see oscillations in macrophage phenotype in the TME. We have focused on CD8 T cells in this study, as they currently represent major therapeutic targets in the clinic. Our data show that antibody administration alters the phenotype of CD8 T cells within the tumor in a time-of-day-dependent manner, already 24 h after the infusion, indicating that these cells are involved in the initial circadian responses. Nevertheless, oscillations in other immune cell lineages that we describe, notably of myeloid cells, may be of additional functional relevance for the circadian effect. The contribution of different immune cell populations in this circadian anti-tumor response remains to be investigated in future studies.

Ultimately, it appears that challenging the immune system with an antibody at a specific time of day not only changes the quantity but also the quality of the response so that the immune system, once stimulated at the "wrong" time, may not be able to respond anymore to the same level and quality as an immune system challenged at the "right" time—just 12 h apart. In an analogous manner to the anti-tumor response described here, a depot effect exists in vaccines, with antigen being present over several days. Yet, time-of-day effects are observed also in vaccination studies, in the pre-clinical setting,[6] and in patients, with higher immune sensitivity present at very similar time windows.[24] The precise mechanisms at play underlying these phenomena remain to be identified.

Sex differences have been reported in cancer immunotherapy, with retrospective analyses indicating that men often respond better compared with women.[45] Of note, with respect to chronoimmunotherapy, subgroup analyses did reveal that women had a particularly high benefit in overall survival with immune checkpoint inhibition infused earlier in the day compared with in the afternoon.[35,46] To what extent and what the mechanisms are will need to be investigated in more detail in future studies. The circadian dynamics in the TME that we uncover here should prove to be of use in the clinic, as tumor biopsies represent currently the main means of assessing the level of immune cell infiltration and defining the ensuing therapeutic regimen. Given that this immune cell infiltration is strongly time-of-day dependent, therapy may differ, depending on when biopsies were performed. Together, we demonstrate in mechanistic detail that TILs exhibit circadian oscillations in both number and phenotype, which can be exploited therapeutically with timed administration of CAR T cells or ICBs.

Limitations of the study

We focused on melanoma in this study, and it remains to be demonstrated in future studies whether this also applies to other tumors. Our observations in mice indicate that at least time-of-day differences in ICB also extend to colon carcinoma. Furthermore, retrospective clinical data indicate that optimization of infusion timing may provide benefits for several types of cancer, including melanoma, NSLSC, and metastatic esophageal squamous cell carcinoma patients. Although our data indicate the optimal time point of infusion to be the evening in mice, the best time point for humans may be the morning hours, given the different periods of behavioral rest and activity in the two species. However, the precise time window remains to be defined, as current data only assessed morning versus afternoon effects.

Although our data indicate that the lineage-specific, inducible deletion of *Bmal1* in endothelial cells affects the oscillatory behavior of these cells and, by extension, the recruitment of leukocytes, there may be additional factors that could contribute to the observed abrogation of time-of-day-dependent leukocyte migration.

STAR★METHODS

Detailed methods are provided in the online version of this paper and include the following:

- KEY RESOURCES TABLE
- RESOURCE AVAILABILITY
  - Lead contact
  - Materials availability
  - Data and code availability
- EXPERIMENTAL MODEL AND STUDY PARTICIPANT DETAILS
  - Animals
- METHOD DETAILS
  - Tumor cell lines and inoculation
  - Mouse T cell activation
  - Mouse T cell synchronization
  - Human $CD8^+$ T cell activation and synchronization
  - Luciferase-expressing $CD8^+$ T cells
  - Tissue digestion and single-cell preparation
  - Flow Cytometry
  - Mouse leukocyte adoptive transfer
  - EdU assay
  - CD8 T cell sorting and RNA extraction
  - RNA extraction, reverse transcription and qPCR
  - *In vivo* antibody treatments
  - Human CAR T cell generation
  - Human CAR T cell adoptive transfer
  - Immunofluorescence imaging
  - Human immunohistochemistry
  - Single cell sequencing and analysis
  - *ZeitZeiger* analysis
  - Estimation of cell composition in TCGA melanoma patients
- QUANTIFICATION AND STATISTICAL ANALYSIS

SUPPLEMENTAL INFORMATION

Supplemental information can be found online at https://doi.org/10.1016/j.cell.2024.04.015.

ACKNOWLEDGMENTS

We thank Urs Albrecht and Jürgen Ripperger for providing *Per1*$^{-/-}$*Per2*$^{-/-}$ mice. We thank the IGE3 Genomics Platform and the flow cytometry core facility of the University of Geneva. We thank Dr. Lydia Lutes, Dr. Laure Garnier, Dr. Flore Sinturel, and Dr. Liqing Cheng for invaluable input and discussions. This study received support from the European Research Council (ERC CoG 101001233, CIRCADYN [C.S.]), the Swiss National Science Foundation (SNSF, 310030_182417/1 [C.S.] and 310030_185255 [S.H.]), the Swiss Cancer League (KLS-4836-08-2019 [C.S.]), the Geneva Cancer League (2106 [C.S.]), the EU ITN (813284, INTEGRATA [C.S.]), and the Fondation privé des HUG (RC05-03 [C.S.]). C.J. is supported by a SNSF PRIMA fellowship (PR00P3_179727), the Swiss Cancer League (KFS 5250-02-2021), and the Geneva Cancer League (GCL, 2007). M.C. is the recipient of an iGE3 PhD salary award. P.-C. Ho received support from the Cancer Research Institute, the Melanoma Research Alliance, the Ludwig Cancer Research, and the Swiss National Science Foundation (310030L_208130). M.J.P. received support

from the ISREC Foundation, Ludwig Cancer Research, and NIH grants P01-CA240239 and R01-CA218579. R.B. was funded by a Postdoc Mobility fellowship and a Return Grant of the SNSF (P400PM_183852 and P5R5PM_203164). Research in the A.D.G. lab is supported by Research Foundation Flanders (FWO) (Fundamental Research Grant, G0B4620N; FWO SBO grant for "ANTIBODY" consortium), KU Leuven (C1 grant, C14/19/098, and C3 grants, C3/21/037 and C3/22/022), Kom op Tegen Kanker (KOTK/2018/11509/1 and KOTK/2019/11955/1), VLIR-UOS (iBOF grant, iBOF/21/048, for "MIMICRY" consortium), and Olivia Hendrickx Research Fund (OHRF Immuunbiomarkers). C.D. was funded by Swiss National Science Foundation grant 310030_184708/1, the Vontobel Foundation, the Novartis Consumer Health Foundation, EFSD/Novo Nordisk Programme for Diabetes Research in Europe, Swiss Life Foundation, the Olga Mayenfisch Foundation, the Fondation pour l'innovation sur le cancer et la biologie, the Ligue Pulmonaire Genevoise, Swiss Cancer League KFS-5266-02-2021-R, the Velux Foundation, the Leenaards Foundation, the ISREC Foundation, and the Gertrude von Meissner Foundation (V.P. and C.D.). Y.W. received support from the Science Foundation of Peking University Cancer Hospital (2022-21). Extended data Figure 6A and the graphical abstract were created with BioRender.

AUTHOR CONTRIBUTIONS

Conceptualization: C.W., Z.L., S.H., C.J., C.D., A.D.G., P.-C. Ho, O.M., F.S., M.J.P., and C.S.; methodology: C.W., Q.Z., P.C., S.N., Z.S., and A.D.G.; investigation: C.W., Q.Z., S.W., R.B., Y.W., C.B., R.P., M.C., M.S., P.-C. Hsueh, S.H.M., S.J., V.P., F.S., Z.L., and Z.M.G.; visualization: C.W., Q.Z., P.C., S.N., A.D.G., and C.S.; supervision: C.S.; writing: C.W., Q.Z., M.J.P., and C.S.

DECLARATION OF INTERESTS

C.S. has been a consultant for Bayer and received speaker fees from Abbvie. M.J.P. has been a consultant for AstraZeneca, Debiopharm, Elstar Therapeutics, ImmuneOncia, KSQ Therapeutics, MaxiVax, Merck, Molecular Partners, Third Rock Ventures, and Tidal. F.S. received consulting fees from BMS/Celgene, Incyte, Kite/Gilead, speaker fees from Kite/Gilead, Incyte, travel support from Kite/Gilead, Novartis, AstraZeneca, Neovii, Janssen, and research funding from Kite/Gilead, Novartis, and BMS/Celgene. A.D.G. received consulting/advisory/lecture honoraria or research funding from Boehringer Ingelheim, SOTIO, Miltenyi Biotec, Novigenix, and IsoPlexis. R.B. received speaker fees from Janssen and is a mentee of the ENDEAVOUR-Breast program of Daichii Sankyo. All these relationships are unrelated to this study.

Received: October 12, 2023
Revised: February 2, 2024
Accepted: April 16, 2024
Published: May 8, 2024

REFERENCES

1. Mellman, I., Coukos, G., and Dranoff, G. (2011). Cancer immunotherapy comes of age. Nature *480*, 480–489. https://doi.org/10.1038/nature10673.
2. Tawbi, H.A., Schadendorf, D., Lipson, E.J., Ascierto, P.A., Matamala, L., Castillo Gutiérrez, E., Rutkowski, P., Gogas, H.J., Lao, C.D., De Menezes, J.J., et al. (2022). Relatlimab and Nivolumab versus Nivolumab in Untreated Advanced Melanoma. N. Engl. J. Med. *386*, 24–34. https://doi.org/10.1056/NEJMoa2109970.
3. Cappell, K.M., and Kochenderfer, J.N. (2023). Long-term outcomes following CAR T cell therapy: what we know so far. Nat. Rev. Clin. Oncol. *20*, 359–371. https://doi.org/10.1038/s41571-023-00754-1.
4. Flugel, C.L., Majzner, R.G., Krenciute, G., Dotti, G., Riddell, S.R., Wagner, D.L., and Abou-El-Enein, M. (2023). Overcoming on-target, off-tumour toxicity of CAR T cell therapy for solid tumours. Nat. Rev. Clin. Oncol. *20*, 49–62. https://doi.org/10.1038/s41571-022-00704-3.
5. Tumeh, P.C., Harview, C.L., Yearley, J.H., Shintaku, I.P., Taylor, E.J.M., Robert, L., Chmielowski, B., Spasic, M., Henry, G., Ciobanu, V., et al. (2014). PD-1 blockade induces responses by inhibiting adaptive immune resistance. Nature *515*, 568–571. https://doi.org/10.1038/nature13954.
6. Wang, C., Barnoud, C., Cenerenti, M., Sun, M., Caffa, I., Kizil, B., Bill, R., Liu, Y., Pick, R., Garnier, L., et al. (2023). Dendritic cells direct circadian anti-tumour immune responses. Nature *614*, 136–143. https://doi.org/10.1038/s41586-022-05605-0.
7. Scheiermann, C., Gibbs, J., Ince, L., and Loudon, A. (2018). Clocking in to immunity. Nat. Rev. Immunol. *18*, 423–437. https://doi.org/10.1038/s41577-018-0008-4.
8. Arjona, A., Silver, A.C., Walker, W.E., and Fikrig, E. (2012). Immunity's fourth dimension: approaching the circadian-immune connection. Trends Immunol. *33*, 607–612. https://doi.org/10.1016/j.it.2012.08.007.
9. Curtis, A.M., Bellet, M.M., Sassone-Corsi, P., and O'Neill, L.A.J. (2014). Circadian clock proteins and immunity. Immunity *40*, 178–186. https://doi.org/10.1016/j.immuni.2014.02.002.
10. Cermakian, N., Stegeman, S.K., Tekade, K., and Labrecque, N. (2022). Circadian rhythms in adaptive immunity and vaccination. Semin. Immunopathol. *44*, 193–207. https://doi.org/10.1007/s00281-021-00903-7.
11. Man, K., Loudon, A., and Chawla, A. (2016). Immunity around the clock. Science *354*, 999–1003. https://doi.org/10.1126/science.aah4966.
12. Palomino-Segura, M., and Hidalgo, A. (2021). Circadian immune circuits. J. Exp. Med. *218*, e20200798. https://doi.org/10.1084/jem.20200798.
13. Wang, C., Lutes, L.K., Barnoud, C., and Scheiermann, C. (2022). The circadian immune system. Sci. Immunol. *7*, eabm2465. https://doi.org/10.1126/sciimmunol.abm2465.
14. He, W., Holtkamp, S., Hergenhan, S.M., Kraus, K., de Juan, A., Weber, J., Bradfield, P., Grenier, J.M.P., Pelletier, J., Druzd, D., et al. (2018). Circadian Expression of Migratory Factors Establishes Lineage-Specific Signatures that Guide the Homing of Leukocyte Subsets to Tissues. Immunity *49*, 1175–1190.e7. https://doi.org/10.1016/j.immuni.2018.10.007.
15. Druzd, D., Matveeva, O., Ince, L., Harrison, U., He, W., Schmal, C., Herzel, H., Tsang, A.H., Kawakami, N., Leliavski, A., et al. (2017). Lymphocyte Circadian Clocks Control Lymph Node Trafficking and Adaptive Immune Responses. Immunity *46*, 120–132. https://doi.org/10.1016/j.immuni.2016.12.011.
16. Shimba, A., Cui, G., Tani-ichi, S., Ogawa, M., Abe, S., Okazaki, F., Kitano, S., Miyachi, H., Yamada, H., Hara, T., et al. (2018). Glucocorticoids Drive Diurnal Oscillations in T Cell Distribution and Responses by Inducing Interleukin-7 Receptor and CXCR4. Immunity *48*, 286–298.e6. https://doi.org/10.1016/j.immuni.2018.01.004.
17. Casanova-Acebes, M., Nicolás-Ávila, J.A., Li, J.L., García-Silva, S., Balachander, A., Rubio-Ponce, A., Weiss, L.A., Adrover, J.M., Burrows, K., A-González, N., et al. (2018). Neutrophils instruct homeostatic and pathological states in naive tissues. J. Exp. Med. *215*, 2778–2795. https://doi.org/10.1084/jem.20181468.
18. Nguyen, K.D., Fentress, S.J., Qiu, Y., Yun, K., Cox, J.S., and Chawla, A. (2013). Circadian gene Bmal1 regulates diurnal oscillations of Ly6C(hi) inflammatory monocytes. Science *341*, 1483–1488. https://doi.org/10.1126/science.1240636.
19. Cervantes-Silva, M.P., Carroll, R.G., Wilk, M.M., Moreira, D., Payet, C.A., O'Siorain, J.R., Cox, S.L., Fagan, L.E., Klavina, P.A., He, Y., et al. (2022). The circadian clock influences T cell responses to vaccination by regulating dendritic cell antigen processing. Nat. Commun. *13*, 7217. https://doi.org/10.1038/s41467-022-34897-z.
20. Ince, L.M., Barnoud, C., Lutes, L.K., Pick, R., Wang, C., Sinturel, F., Chen, C.S., de Juan, A., Weber, J., Holtkamp, S.J., et al. (2023). Influence of circadian clocks on adaptive immunity and vaccination responses. Nat. Commun. *14*, 476. https://doi.org/10.1038/s41467-023-35979-2.
21. Nobis, C.C., Dubeau Laramée, G., Kervezee, L., Maurice De Sousa, D., Labrecque, N., and Cermakian, N. (2019). The circadian clock of CD8 T cells modulates their early response to vaccination and the rhythmicity of related signaling pathways. Proc. Natl. Acad. Sci. USA *116*, 20077–20086. https://doi.org/10.1073/pnas.1905080116.

22. Gibbs, J., Ince, L., Matthews, L., Mei, J., Bell, T., Yang, N., Saer, B., Begley, N., Poolman, T., Pariollaud, M., et al. (2014). An epithelial circadian clock controls pulmonary inflammation and glucocorticoid action. Nat. Med. *20*, 919–926. https://doi.org/10.1038/nm.3599.

23. Scheiermann, C., Kunisaki, Y., Lucas, D., Chow, A., Jang, J.E., Zhang, D., Hashimoto, D., Merad, M., and Frenette, P.S. (2012). Adrenergic nerves govern circadian leukocyte recruitment to tissues. Immunity *37*, 290–301. https://doi.org/10.1016/j.immuni.2012.05.021.

24. Hazan, G., Duek, O.A., Alapi, H., Mok, H., Ganninger, A., Ostendorf, E., Gierasch, C., Chodick, G., Greenberg, D., and Haspel, J.A. (2023). Biological rhythms in COVID-19 vaccine effectiveness in an observational cohort study of 1.5 million patients. J. Clin. Invest. *133*, e167339. https://doi.org/10.1172/JCI167339.

25. Long, J.E., Drayson, M.T., Taylor, A.E., Toellner, K.M., Lord, J.M., and Phillips, A.C. (2016). Morning vaccination enhances antibody response over afternoon vaccination: A cluster-randomised trial. Vaccine *34*, 2679–2685. https://doi.org/10.1016/j.vaccine.2016.04.032.

26. Ho, P.C., Bihuniak, J.D., Macintyre, A.N., Staron, M., Liu, X., Amezquita, R., Tsui, Y.C., Cui, G., Micevic, G., Perales, J.C., et al. (2015). Phosphoenolpyruvate Is a Metabolic Checkpoint of Anti-tumor T Cell Responses. Cell *162*, 1217–1228. https://doi.org/10.1016/j.cell.2015.08.012.

27. Raskov, H., Orhan, A., Christensen, J.P., and Gögenur, I. (2021). Cytotoxic CD8+ T cells in cancer and cancer immunotherapy. Br. J. Cancer *124*, 359–367. https://doi.org/10.1038/s41416-020-01048-4.

28. National Comprehensive Cancer Network (2024). B-Cell Lymphomas. https://www.nccn.org/guidelines/guidelines-detail?category=1&id=1480.

29. Neelapu, S.S., Dickinson, M., Munoz, J., Ulrickson, M.L., Thieblemont, C., Oluwole, O.O., Herrera, A.F., Ujjani, C.S., Lin, Y., Riedell, P.A., et al. (2022). Axicabtagene ciloleucel as first-line therapy in high-risk large B-cell lymphoma: the phase 2 ZUMA-12 trial. Nat. Med. *28*, 735–742. https://doi.org/10.1038/s41591-022-01731-4.

30. Arjona, A., and Sarkar, D.K. (2005). Circadian oscillations of clock genes, cytolytic factors, and cytokines in rat NK cells. J. Immunol. *174*, 7618–7624. https://doi.org/10.4049/jimmunol.174.12.7618.

31. Hughey, J.J., Hastie, T., and Butte, A.J. (2016). ZeitZeiger: supervised learning for high-dimensional data from an oscillatory system. Nucleic Acids Res. *44*, e80. https://doi.org/10.1093/nar/gkw030.

32. Zhao, Y., Liu, M., Chan, X.Y., Tan, S.Y., Subramaniam, S., Fan, Y., Loh, E., Chang, K.T.E., Tan, T.C., and Chen, Q. (2017). Uncovering the mystery of opposite circadian rhythms between mouse and human leukocytes in humanized mice. Blood *130*, 1995–2005. https://doi.org/10.1182/blood-2017-04-778779.

33. Sade-Feldman, M., Yizhak, K., Bjorgaard, S.L., Ray, J.P., de Boer, C.G., Jenkins, R.W., Lieb, D.J., Chen, J.H., Frederick, D.T., Barzily-Rokni, M., et al. (2018). Defining T Cell States Associated with Response to Checkpoint Immunotherapy in Melanoma. Cell *175*, 998–1013.e20. https://doi.org/10.1016/j.cell.2018.10.038.

34. Naulaerts, S., Datsi, A., Borras, D.M., Antoranz Martinez, A., Messiaen, J., Vanmeerbeek, I., Sprooten, J., Laureano, R.S., Govaerts, J., Panovska, D., et al. (2023). Multiomics and spatial mapping characterizes human $CD8^+$ T cell states in cancer. Sci. Transl. Med. *15*, eadd1016. https://doi.org/10.1126/scitranslmed.add1016.

35. Qian, D.C., Kleber, T., Brammer, B., Xu, K.M., Switchenko, J.M., Janopaul-Naylor, J.R., Zhong, J., Yushak, M.L., Harvey, R.D., Paulos, C.M., et al. (2021). Effect of immunotherapy time-of-day infusion on overall survival among patients with advanced melanoma in the USA (MEMOIR): a propensity score-matched analysis of a single-centre, longitudinal study. Lancet Oncol. *22*, 1777–1786. https://doi.org/10.1016/S1470-2045(21)00546-5.

36. Yeung, C., Kartolo, A., Tong, J., Hopman, W., and Baetz, T. (2023). Association of circadian timing of initial infusions of immune checkpoint inhibitors with survival in advanced melanoma. Immunotherapy *15*, 819–826. https://doi.org/10.2217/imt-2022-0139.

37. Gonçalves, L., Gonçalves, D., Esteban-Casanelles, T., Barroso, T., Soares de Pinho, I., Lopes-Brás, R., Esperança-Martins, M., Patel, V., Torres, S., Teixeira de Sousa, R., et al. (2023). Immunotherapy around the Clock: Impact of Infusion Timing on Stage IV Melanoma Outcomes. Cells *12*, 2068. https://doi.org/10.3390/cells12162068.

38. Karaboué, A., Collon, T., Pavese, I., Bodiguel, V., Cucherousset, J., Zakine, E., Innominato, P.F., Bouchahda, M., Adam, R., and Lévi, F. (2022). Time-Dependent Efficacy of Checkpoint Inhibitor Nivolumab: Results from a Pilot Study in Patients with Metastatic Non-Small-Cell Lung Cancer. Cancers (Basel) *14*, 896. https://doi.org/10.3390/cancers14040896.

39. Rousseau, A., Tagliamento, M., Auclin, E., Aldea, M., Frelaut, M., Levy, A., Benitez, J.C., Naltet, C., Lavaud, P., Botticella, A., et al. (2023). Clinical outcomes by infusion timing of immune checkpoint inhibitors in patients with advanced non-small cell lung cancer. Eur. J. Cancer *182*, 107–114. https://doi.org/10.1016/j.ejca.2023.01.007.

40. Nomura, M., Hosokai, T., Tamaoki, M., Yokoyama, A., Matsumoto, S., and Muto, M. (2023). Timing of the infusion of nivolumab for patients with recurrent or metastatic squamous cell carcinoma of the esophagus influences its efficacy. Esophagus *20*, 722–731. https://doi.org/10.1007/s10388-023-01006-y.

41. Landré, T., Karaboué, A., Buchwald, Z.S., Innominato, P.F., Qian, D.C., Assié, J.B., Chouaïd, C., Lévi, F., and Duchemann, B. (2024). Effect of immunotherapy-infusion time of day on survival of patients with advanced cancers: a study-level meta-analysis. ESMO Open *9*, 102220. https://doi.org/10.1016/j.esmoop.2023.102220.

42. Martin, A.M., Cagney, D.N., Catalano, P.J., Alexander, B.M., Redig, A.J., Schoenfeld, J.D., and Aizer, A.A. (2018). Immunotherapy and Symptomatic Radiation Necrosis in Patients With Brain Metastases Treated With Stereotactic Radiation. JAMA Oncol. *4*, 1123–1124. https://doi.org/10.1001/jamaoncol.2017.3993.

43. Postow, M.A., Goldman, D.A., Shoushtari, A.N., Betof Warner, A., Callahan, M.K., Momtaz, P., Smithy, J.W., Naito, E., Cugliari, M.K., Raber, V., et al. (2022). Adaptive Dosing of Nivolumab + Ipilimumab Immunotherapy Based Upon Early, Interim Radiographic Assessment in Advanced Melanoma (The ADAPT-IT Study). J. Clin. Oncol. *40*, 1059–1067. https://doi.org/10.1200/JCO.21.01570.

44. Arlauckas, S.P., Garris, C.S., Kohler, R.H., Kitaoka, M., Cuccarese, M.F., Yang, K.S., Miller, M.A., Carlson, J.C., Freeman, G.J., Anthony, R.M., et al. (2017). In vivo imaging reveals a tumor-associated macrophage-mediated resistance pathway in anti-PD-1 therapy. Sci. Transl. Med. *9*, eaal3604. https://doi.org/10.1126/scitranslmed.aal3604.

45. Conforti, F., Pala, L., Bagnardi, V., De Pas, T., Martinetti, M., Viale, G., Gelber, R.D., and Goldhirsch, A. (2018). Cancer immunotherapy efficacy and patients' sex: a systematic review and meta-analysis. Lancet Oncol. *19*, 737–746. https://doi.org/10.1016/S1470-2045(18)30261-4.

46. Lévi, F.A., Okyar, A., Hadadi, E., Innominato, P.F., and Ballesta, A. (2024). Circadian Regulation of Drug Responses: Toward Sex-Specific and Personalized Chronotherapy. Annu. Rev. Pharmacol. Toxicol. *64*, 89–114. https://doi.org/10.1146/annurev-pharmtox-051920-095416.

47. Duan, J., Ngo, M.N., Karri, S.S., Tsoi, L.C., Gudjonsson, J.E., Shahbaba, B., Lowengrub, J., and Andersen, B. (2023). tauFisher accurately predicts circadian time from a single sample of bulk and single-cell transcriptomic data. Preprint at bioRxiv. https://doi.org/10.1101/2023.04.04.535473.

48. Welz, P.-S., Zinna, V.M., Symeonidi, A., Koronowski, K.B., Kinouchi, K., Smith, J.G., Guillén, I.M., Castellanos, A., Furrow, S., Aragón, F., et al. (2019). BMAL1-Driven Tissue Clocks Respond Independently to Light to Maintain Homeostasis. Cell *177*, 1436–1447.e12. https://doi.org/10.1016/j.cell.2019.05.009.

49. Wang, H., van Spyk, E., Liu, Q., Geyfman, M., Salmans, M.L., Kumar, V., Ihler, A., Li, N., Takahashi, J.S., and Andersen, B. (2017). Time-Restricted Feeding Shifts the Skin Circadian Clock and Alters UVB-Induced DNA Damage. Cell Rep. *20*, 1061–1072. https://doi.org/10.1016/j.celrep.2017.07.022.

50. Tsujihana, K., Tanegashima, K., Santo, Y., Yamada, H., Akazawa, S., Nakao, R., Tominaga, K., Saito, R., Nishito, Y., Hata, R.-I., et al. (2022). Circadian protection against bacterial skin infection by epidermal CXCL14-mediated innate immunity. Proc. Natl. Acad. Sci. USA *119*, e2116027119. https://doi.org/10.1073/pnas.2116027119.

51. Geyfman, M., Kumar, V., Liu, Q., Ruiz, R., Gordon, W., Espitia, F., Cam, E., Millar, S.E., Smyth, P., Ihler, A., et al. (2012). Brain and muscle Arnt-like protein-1 (BMAL1) controls circadian cell proliferation and susceptibility to UVB-induced DNA damage in the epidermis. Proc. Natl. Acad. Sci. USA *109*, 11758–11763. https://doi.org/10.1073/pnas.1209592109.

52. Spörl, F., Korge, S., Jürchott, K., Wunderskirchner, M., Schellenberg, K., Heins, S., Specht, A., Stoll, C., Klemz, R., Maier, B., et al. (2012). Krüppel-like factor 9 is a circadian transcription factor in human epidermis that controls proliferation of keratinocytes. Proc. Natl. Acad. Sci. USA *109*, 10903–10908. https://doi.org/10.1073/pnas.1118641109.

53. del Olmo, M., Spörl, F., Korge, S., Jürchott, K., Felten, M., Grudziecki, A., de Zeeuw, J., Nowozin, C., Reuter, H., Blatt, T., et al. (2022). Inter-layer and inter-subject variability of diurnal gene expression in human skin. NAR Genom. Bioinform. *4*, lqac097. https://doi.org/10.1093/nargab/lqac097.

54. Wu, G., Ruben, M.D., Schmidt, R.E., Francey, L.J., Smith, D.F., Anafi, R.C., Hughey, J.J., Tasseff, R., Sherrill, J.D., Oblong, J.E., et al. (2018). Population-level rhythms in human skin with implications for circadian medicine. Proc. Natl. Acad. Sci. USA *115*, 12313–12318. https://doi.org/10.1073/pnas.1809442115.

55. Sherrill, J.D., Finlay, D., Binder, R.L., Robinson, M.K., Wei, X., Tiesman, J.P., Flagler, M.J., Zhao, W., Miller, C., Loftus, J.M., et al. (2021). Transcriptomic analysis of human skin wound healing and rejuvenation following ablative fractional laser treatment. PLoS One *16*, e0260095. https://doi.org/10.1371/journal.pone.0260095.

56. Hao, Y., Hao, S., Andersen-Nissen, E., Mauck, W.M., 3rd, Zheng, S., Butler, A., Lee, M.J., Wilk, A.J., Darby, C., Zager, M., et al. (2021). Integrated analysis of multimodal single-cell data. Cell *184*, 3573–3587.e29. https://doi.org/10.1016/j.cell.2021.04.048.

57. Wu, T., Hu, E., Xu, S., Chen, M., Guo, P., Dai, Z., Feng, T., Zhou, L., Tang, W., Zhan, L., et al. (2021). clusterProfiler 4.0: A universal enrichment tool for interpreting omics data. Innovation (Camb) *2*, 100141. https://doi.org/10.1016/j.xinn.2021.100141.

58. Carlucci, M., Kriščiūnas, A., Li, H., Gibas, P., Koncevičius, K., Petronis, A., and Oh, G. (2019). DiscoRhythm: an easy-to-use web application and R package for discovering rhythmicity. Bioinformatics *36*, 1952–1954. https://doi.org/10.1093/bioinformatics/btz834.

59. Hänzelmann, S., Castelo, R., and Guinney, J. (2013). GSVA: gene set variation analysis for microarray and RNA-seq data. BMC Bioinformatics *14*, 7. https://doi.org/10.1186/1471-2105-14-7.

60. Colaprico, A., Silva, T.C., Olsen, C., Garofano, L., Cava, C., Garolini, D., Sabedot, T.S., Malta, T.M., Pagnotta, S.M., Castiglioni, I., et al. (2016). TCGAbiolinks: an R/Bioconductor package for integrative analysis of TCGA data. Nucleic Acids Res. *44*, e71. https://doi.org/10.1093/nar/gkv1507.

61. Leek, J.T., Johnson, W.E., Parker, H.S., Jaffe, A.E., and Storey, J.D. (2012). The sva package for removing batch effects and other unwanted variation in high-throughput experiments. Bioinformatics *28*, 882–883. https://doi.org/10.1093/bioinformatics/bts034.

62. Holtkamp, S.J., Ince, L.M., Barnoud, C., Schmitt, M.T., Sinturel, F., Pilorz, V., Pick, R., Jemelin, S., Mühlstädt, M., Boehncke, W.H., et al. (2021). Circadian clocks guide dendritic cells into skin lymphatics. Nat. Immunol. *22*, 1375–1381. https://doi.org/10.1038/s41590-021-01040-x.

63. Wittenbrink, N., Ananthasubramaniam, B., Münch, M., Koller, B., Maier, B., Weschke, C., Bes, F., de Zeeuw, J., Nowozin, C., Wahnschaffe, A., et al. (2018). High-accuracy determination of internal circadian time from a single blood sample. J. Clin. Invest. *128*, 3826–3839. https://doi.org/10.1172/JCI120874.

64. Newman, A.M., Steen, C.B., Liu, C.L., Gentles, A.J., Chaudhuri, A.A., Scherer, F., Khodadoust, M.S., Esfahani, M.S., Luca, B.A., Steiner, D., et al. (2019). Determining cell type abundance and expression from bulk tissues with digital cytometry. Nat. Biotechnol. *37*, 773–782. https://doi.org/10.1038/s41587-019-0114-2.

STAR★METHODS

KEY RESOURCES TABLE

REAGENT or RESOURCE	SOURCE	IDENTIFIER
Antibodies		
Anti-mouse CD45 clone 30-F11	BD Biosciences	564279/AB_2651134
Anti-mouse CD3e clone KT3.1.1	BioLegend	155617/AB_2832541
Anti-mouse CD4 clone GK1.5	BD Biosciences	563232/AB_2738083
Anti-mouse CD8a clone 53-6.7	BD Biosciences	563152/AB_2738030
Anti-mouse CD11c clone N418	BioLegend	117307/AB_313776
Anti-mouse CD19 clone 1D3	BD Biosciences	566412/AB_2744315
Anti-mouse NK1.1 clone PK136	BioLegend	108715/AB_493591
Anti-mouse MHCII clone M5/114.15.2	BioLegend	107643/AB_2565976
Anti-mouse Ly6G clone 1A8	BioLegend	127645/AB_2566317
Anti-mouse Ly6C clone HK1.4	BioLegend	128023/AB_10640119
Anti-mouse CD137 clone 17B5	BioLegend	106106/AB_2287565
Anti-mouse CD107a clone 1D4B	BioLegend	121610/AB_571991
Anti-mouse PD-1clone 29F.1A12	BioLegend	135213/AB_10689633
Anti-mouse Granzyme B clone QA16A02	BioLegend	372207/AB_2687031
Anti-mouse IFN-γ clone XMG1.2	BioLegend	505837/AB_11219004
Anti-mouse CD31 clone MEC13.3,	BioLegend	102520/AB_2563319
Anti-mouse CD4 clone, GK1.5	BioLegend	100405/AB_312690
Anti-mouse CD54 clone, YN1/1.7.4	BioLegend	116114/AB_493495
Anti-mouse CD8 clone 53-6.7	BioLegend	100724/AB_389326
Anti-mouse VCAM-1 clone 429	BioLegend	105710/AB_493427
Anti-mouse anti-CD11a clone M17/4	BioXCell	BE0006/ AB_1107578
Anti-mouse anti-CD18 clone M18/2	BioXCell	BE0009/ AB_1107607
Anti-mouse PD-1, clone 29F.1A12™	BioXCell	BE0273/ AB_2687796
Anti-mouse CD8a, clone YTS 169.4	BioXCell	BE0117/ AB_10950145
Anti-mouse E-selectin clone UZ6	Invitrogen	MA1-06506/ AB_2186701
Anti-human CD3 clone BW264/56	Miltenyi Biotec	130-113-687/AB_2726228
Anti-human CD8 clone RPA-T8	BD Biosciences	563795/AB_2722501
Anti-human CD4 clone SK3	BD Biosciences	565995/AB_2739446
Anti-human CD19 clone HIB19	BioLegend	302219/AB_389313
Anti-human CD4 clone EP204	Zhongshan Golden Bridge Biotechnology	ZA-0519
Anti-human CD8 clone SP16	Zhongshan Golden Bridge Biotechnology	ZA-0508
rat IgG2a isotype control, clone 2A3	BioXCell	BE0089/ AB_1107769
rat IgG2b isotype control, clone LTF-2	BioXCell	BE0090/ AB_1107780
Dynabeads human T-Activator CD3/CD28	Gibco	11132D/AB_2916088
Anti-human CD3 clone BW264/56	BioLegend	317348/ AB_2571995
Dynabeads™ Mouse T-Activator CD3/ CD28 for T-Cell Expansion and Activation	Gibco	11453D
Goat anti-Rat IgG (H+L) Cross-Adsorbed Secondary Antibody	Invitrogen	A21247/ AB_141778
Chemicals, peptides, and recombinant proteins		
DRAQ7	Biolegend	424001
Counting Beads	ThermoFisher	C36950

(*Continued on next page*)

Continued

REAGENT or RESOURCE	SOURCE	IDENTIFIER
eBioscience™ Fixable Viability Dye eFluor™ 780	eBioscience™	65-0865-18
Foxp3 / Transcription Factor Staining Buffer Set	eBioscience™	00-5523-00
Phorbol 12-myristate 13-acetate	Sigma-Aldrich	P1585
Ionomycin	Sigma-Aldrich	I3909
GolgiPlug™	BD Biosciences	555029
CellEvent™ Caspase-3/7 Green Ready Flow™ Reagent	Invitrogen	R37167
CellTracker™ Deep Red Dye	Invitrogen	C34565
RBC lysis buffer	Biolegend	420302
EdU Alexa Fluor™ 594 Flow Cytometry Assay Kit	Invitrogen	C10646
Trizol Reagent	Invitrogen	15596018
Human IL-2	PeproTech	200-02
Mouse IL-2	Biolegend	575406
retronectin	Takara	T100B
streptavidin	Biolegend	405207
biotinylated protein L	ThermoFisher	29997
Collagenase IV	Worthington Biochemical Corporation	LS004189
Collagenase D	Roche	11088866001
DNase I	Roche	04716728001
DAPI	Biolegend	422801
BlockAid™ Blocking Solution	Invitrogen	B10710
Bond Polymer Refine Red Detection kit	Leica	DS9390
Critical commercial assays		
Chromium Single Cell 3′ v3.1 Reagent Kit with dual indexes	10x Genomics	1000269
CD8+ T Cell Isolation Kit, human	Miltenyi Biotec	130-096-495
CD8a+ T Cell Isolation Kit, mouse	Miltenyi Biotec	130-104-075
Deposited data		
Timed scRNA-seq of TILs from murine melanoma	This paper	GEO: GSE260641
Mouse epidermal scRNA-seq	Duan et al.[47]	GEO: GSE223109
Mouse skin RNA-seq	Welz et al.[48]	GEO: GSE115104, GSE114943
Mouse skin RNA-seq	Wang et al.[49]	GEO: GSE83855
Mouse epidermal RNA-seq in constant darkness	Tsujihana et al.[50]	GEO: GSE174155
Mouse skin microarray	Geyfman et al.[51]	GEO: GSE38622, GSE38623
Human epidermal suction blister microarray	Spörl et al.[52]	GEO: GSE35635
Human skin microarray	del Olmo et al.[53]	GEO: GSE205155
Human forearm skin microarray	Wu et al.[54]	GEO: GSE112660
Human skin microarray (fractional laser treatment)	Sherrill et al.[55]	GEO: GSE139305
Human melanoma scRNA-seq	Sade-Feldman et al.[33]	GEO: GSE120575
Other supporting data	This paper	(https://doi.org/10.26037/yareta:5rmtlmd5sreo7bmcbe44bbijfm).
Experimental models: Cell lines		
B16-F10-OVA	Stéphanie Hugues, UNIGE, Switzerland	N/A

(*Continued on next page*)

Continued

REAGENT or RESOURCE	SOURCE	IDENTIFIER
Murine MC38 colorectal carcinoma cell line	Mark J. Smyth	RRID: CVCL_B288
Human lymphoma DoHH2	Francesco Bertoni, IOR,Bellinzona, Switzerland	N/A
Experimental models: Organisms/strains		
Mouse: WT C57BL/6J	The Jackson Laboratory	Strain # 000664 RRID:IMSR_JAX:000664
Mouse: WT C57BL/6N	Charles River	Strain # CRL027 RRID:IMSR_CRL:027
Mouse: B6.129S4(Cg)-Bmal1tm1Weit/J	The Jackson Laboratory	Strain #:007668 RRID:IMSR_JAX:007668
Mouse: B6.Cg-Tg(Cd4-cre)1Cwi/BfluJ	The Jackson Laboratory	Strain #:022071 RRID:IMSR_JAX:022071
Cdh5-cre/ERT2 mice	Ralf Adams, MPI Munster, Germany	N/A
NSG (NOD.Cg-PrkdcscidIL2rgtm1Wjl/SzJ)	Charles River	Strain #:614
$BRaf^{CA}$, $Pten^{loxP}$, Tyr::CreERT2	Ping-Chih Ho, UNIL, Switzerland	He et al.[14]
CD45.1 OT-I	Walter Reith, UNIGE, Switzerland	N/A
Oligonucleotides		
Mouse Pdcd1 F CGGTTTCAAGGCATGGTCATTGG	Microsynth	N/A
Mouse Pdcd1 R *TCAGAGTGTCGTCCTTGCTTCC*	Microsynth	N/A
Mouse *Rplp0 F GAGACTGAGTACACCTTCCCAC*	Microsynth	N/A
Mouse *Rplp0 R ATGCAGATGGATCAGCCAGG*	Microsynth	N/A
Mouse *Rpl32 F ACAATGTCAAGGAGCTGGAG*	Microsynth	N/A
Mouse *Rpl32 R TTGGGATTGGTGACTCTGATG*	Microsynth	N/A
Human PDCD1-F CCAGGATGGTTCTTAGACTCCC	Microsynth	N/A
Human *PDCD1-R TTTAGCACGAAGCTCTCCGAT*	Microsynth	N/A
Human *Rplp0 F TGGTCATCCAGCAGGTGTTCGA*	Microsynth	N/A
Human *Rplp0 R ACAGACACTGGCAACATTGCGG*	Microsynth	N/A
Software and algorithms		
FACSDiva 6	BD Biosciences	RRID:SCR_001456
FlowJo 10	BD Biosciences	RRID:SCR_008520
Slidebook	3i	RRID:SCR_014300
ImageJ	FIJI	RRID:SCR_002285
Cell Ranger 6.1.2	10X Genomics	RRID:SCR_017344
Seurat 4.3.0	Hao et al.[56]	https://satijalab.org/seurat/
R 4.2.2	The R Foundation	https://www.r-project.org/
clusterProfiler	Wu et al.[57]	https://bioconductor.org/packages/release/bioc/html/clusterProfiler.html
Cosinor	Open source	https://github.com/sachsmc/cosinor
DiscoRhythm	Carlucci et al.[58]	https://bioconductor.org/packages/release/bioc/html/DiscoRhythm.html
GSVA	Hanzelmann et al.[59]	https://bioconductor.org/packages/release/bioc/html/GSVA.html

(*Continued on next page*)

Continued

REAGENT or RESOURCE	SOURCE	IDENTIFIER
TCGAbiolinks	Colaprico et al.[60]	https://bioconductor.org/packages/release/bioc/html/TCGAbiolinks.html
zeitZeiger	Hughey et al.[31]	https://github.com/hugheylab/zeitzeiger
sva	Leek et al.[61]	https://bioconductor.org/packages/release/bioc/html/sva.html
Analysis code	This study	https://github.com/zqun1/circadian_immune_mouse_melanoma

RESOURCE AVAILABILITY

Lead contact

Further information and requests for resources or reagents should be directed to and will be fulfilled by the lead contact, Christoph Scheiermann (christoph.scheiermann@unige.ch).

Materials availability

This study did not generate new unique reagents.

Data and code availability

- Single-cell RNA-seq data have been deposited at GEO: GSE260641 and are publicly available as of the date of publication. Accession numbers of public data used in this study are listed in the key resources table. All data supporting the conclusions of this paper are available online (https://doi.org/10.26037/yareta:5rmtlmd5sreo7bmcbe44bbijfm).
- All original code has been deposited at GitHub https://github.com/zqun1/circadian_immune_mouse_melanoma and is publicly available as of the date of publication.
- Any additional information required to reanalyze the data reported in this paper is available from the lead contact upon request.

EXPERIMENTAL MODEL AND STUDY PARTICIPANT DETAILS

Animals

C57BL/6 and NSG mice were purchased from Charles River or the Jackson Laboratory. Transgenic mouse lines *Bmal1*$^{flox/flox}$, *Cd4*^{Cre} (purchased from Jackson Labs) and *Cdh5*^{CreERT2} (gift from Dr. Ralf Adams, Max-Planck-Institute for Molecular Biomedicine Münster, Germany) were crossed and bred at ENVIGO. Transgenic mice were maintained as homozygous for *Bmal1*$^{flox/flox}$ and heterozygous for the relevant Cre. CD45.1 OT-I (gift from Walter Reith) mice were bred in house. All mice used were at 8-12 weeks of age. Cre recombination in *Cdh5*^{CreERT2} mice was induced by intraperitoneal injection of tamoxifen (1mg per injection) for 5 consecutive days. Unless specified, mice were housed under a 12 h:12 h light:dark schedule with food and water *ad libitum*. When multiple time points were investigated simultaneously, light-tight cabinets (Techniplast) were used to shift animals to the respective phase prior to the experiments. Treatment times correspond to *Zeitgeber* time (ZT) and indicate timing relative to lights on in the animal facility such that ZT1 is 1 h after lights on (morning), and ZT13 is 1 h after lights off (evening). A spontaneous tumor model was induced in *BRaf*^{CA}, *Pten*^{loxP}, *Tyr::CreERT2* mice as previously described[26] by topically treatment with 1 μl 4-hydroxytamoxifen (8 mg/μl in ethanol) on the skin surface. During the dark phase, all manipulations were performed under dim red light. All animal procedures and experiments were approved and performed in accordance with the guidelines of the animal research committee of Geneva, Switzerland, the veterinary authority of Canton de Vaud, Switzerland, or the MGH Institutional Animal Care and Use Committee (IACUC) and were performed in accordance with MGH IACUC regulations.

METHOD DETAILS

Tumor cell lines and inoculation

Mouse melanoma cell lines B16-F10 (ATCC) and B16-F10-OVA (gift from Stéphanie Hugues, University of Geneva, Switzerland) were maintained in RPMI (Gibco) supplemented with 10% heat-inactivated FCS (Gibco), 100 μmol/L penicillin–streptomycin (Gibco), and 50 mmol/L of β-mercaptoethanol (Gibco). MC38 murine colon adenocarcinoma cells (gift from Mikaël Pittet, University of Geneva, Switzerland) were maintained in DMEM (Gibco), 10% heat-inactivated FCS and 100 μmol/L penicillin–streptomycin). Cell lines were used by passage 10 and tested negative for *Mycoplasma*. Unless otherwise specified, 5×10^5 tumor cells in 100μl PBS were injected s.c. into the right flank of mice, under isoflurane anesthesia. For anti-PD-1 therapy experiment, 2×10^5 tumor cells in 100μl PBS or 2×10^6 (MC-38) in 100μl PBS were injected s.c. Human lymphoma DoHH2 cell line (gift from Francesco Bertoni, Institute

of Oncology Research (IOR), Bellinzona, Switzerland) were cultured in RPMI (Gibco) supplemented with 10% heat-inactivated FCS (Gibco). A total of 5×10^6 cells were injected s.c. into the right flank of NSG mice. Tumor volume was monitored every 1 to 2 days using a caliper and calculated by length × width× width/2.

Mouse T cell activation

Splenocytes from C57BL/6 wild type mice, *Cd4cre:Bmal1^{flox}* and their littermate controls, or OT-I mice were collected by smashing the spleen through a 70-μm mesh cell strainer. Red blood cells were lysed using RBC lysis buffer (Biolegend, 420302) for 5 min on ice. To activate CD8$^+$ T cells from C57BL/6 or *Cd4cre:Bmal1^{flox}* mice, CD8$^+$ T cells were enriched using a cell isolation kit (Miltenyi) according to the manufacturer's instructions. The isolated T cells were counted and resuspended in a concentration of 1×10^6/ml in T cell complete medium (RPMI, 10% heat-inactivated FCS, 2 mM L-glutamine, 1% penicillin-streptomycin, 50 μM β-mercaptoethanol, 1mM pyruvate sodium) supplemented with 100U/mL mouse interleukin-2 (IL-2) (Biolegend) in 24-well plate. Dynabeads™ Mouse T-Activator CD3/CD28 beads (Gibco, 11452D) were used to activate T cells according to the manufacturer's instructions. For OT-I cell activation, whole splenocytes were resuspended in a concentration of 1×10^6/ml in T cell complete medium (RPMI, 10% heat-inactivated FCS, 2 mM L-glutamine, 1% penicillin-streptomycin, 50 μM β-mercaptoethanol, 1mM pyruvate sodium) supplemented with 100U/mL mouse interleukin-2 (IL-2) (Biolegend) and 1 nM of OVA257-264 peptide (SIINFEKL, InvivoGen) in a 6-well plate. After 3 days of activation, CD8$^+$ T cells were collected and purified by removing Dynabeads (for polyclonal cells) or using a CD8$^+$ T cell isolation kit (Miltenyi) (for OT-I). For *in vivo* experiments, 1×10^6 OT-I cells were injected intravenously (i.v) into tumor-bearing mice.

Mouse T cell synchronization

Cells were synchronized using horse serum as previously described.[6,21,62] In brief, activated T cells (as described above) were collected and seeded into 24-well plate with a density of 2×10^5/ml in T cell complete medium, supplemented with 100U/mL mouse interleukin-2 (IL-2) (Biolegend) and 0.1μg/mL anti-mouse CD3 antibody (Invitrogen, 16-0031-85) to maintain the TCR signal. An equal volume of horse serum (Sigma, h1270) was pre-warmed and added directly to the plate (serum shock). After 2h incubation at 37°C with 5% CO2, cells were washed and resuspended in T cell complete medium with IL-2 and anti-CD3 antibody.

Human CD8$^+$ T cell activation and synchronization

Human CD8$^+$ T cells were isolated using CD8$^+$ T Cell Isolation Kit (Miltenyi 130-096-495) from the peripheral blood mononuclear cells from healthy donors' buffy coat (provided by University Hospitals of Geneva (HUG), Switzerland) using Ficoll-Paque Plus (Cytiva). Cells were resuspended at $1x10^6$/ml and activated for 3 days with Dynabeads human T-Activator CD3/CD28 (Gibco, 11132D) in the presence of recombinant human IL-2 (50 U/mL, PeproTech, 200-02) in T cell complete medium at 37°C with 5% CO2. Cells were synchronized using horse serum as described above, supplemented with 50U/mL human IL-2 and 0.1μg/mL anti-human CD3 antibody (Invitrogen, Clone OKT3, 16-0037-81).

Luciferase-expressing CD8$^+$ T cells

CD8$^+$ T cells were isolated from the spleen of *Per2::Luc* mice and activated as described above. Activated CD8$^+$ T cells were synchronized and resuspended at 2×10^5/ml in 2 ml T cell complete medium containing 100 μM luciferin (Abcam, ab45164). Dishes were sealed with parafilm and recorded using a LumiCycle detector (Actimetrics).

Tissue digestion and single-cell preparation

Tumor tissue was collected and chopped into small pieces, digestion medium was added (RPMI containing 1mg/mL collagenase IV (Worthington Biochemical Corporation), 40 μg/mL DNase I (Roche 04716728001) and 2% heat-inactivated FCS) and incubated for 30 minutes at 37 °C. Cells were rinsed through a 70 μm cell strainer to obtain single-cell suspensions. To remove debris, Lymphoprep™ (CEDARLANE) was used according to manufacturer's instructions.

Flow Cytometry

Single-cell suspensions were prepared and incubated with mouse or human Fc receptor block (anti-mouse CD16/32 Biolegend, human FcR blocking reagent, Miltenyi Biotec) for 10 minutes at room temperature (RT). After incubation, unless specified otherwise, the antibody mix was added directly into the cell suspension and incubated for 15 min at 4°C.

Cells were washed and resuspended in 300 μl FACs buffer with viability dye (DRAQ7, Biolegend, 2 μM) and characterized using an 18-colour BD LSR Fortessa (BD Biosciences) or Beckman Coulter Cytoflex. Acquired data were analyzed using FACSDiva 6 (BD Biosciences) and FlowJo 10 (BD). Cell counts were calculated using Counting Beads (C36950, C36995, ThermoFisher).

For intracellular staining, cells were stained with viability dye (eBioscience™ Fixable Viability Dye eFluor™ 780, 65-0865-18), followed by surface staining as previously described.[6] Cells were fixed and permeabilized using Foxp3 / Transcription Factor Staining Buffer Set (eBioscience, 00-5523-00). Upon wash with permeabilization buffer, the intracellular antibody was added and incubated for 30 min at room temperature. The following antibodies were used for intracellular staining: anti-mouse Granzyme and anti-mouse IFN-γ. For cytokine detection (Granzyme B, IFN-γ), cells were stimulated before staining in complete RPMI medium with phorbol 12-myristate 13-acetate (PMA, 100 ng/ml; Sigma-Aldrich), ionomycin (1 μg/ml; Sigma-Aldrich), and BD GolgiPlug™ (1:1000; BD

Biosciences, 555029) and incubated 4 hours at 37°C, 5% CO2. Caspase-3/7 detection was performed using CellEvent™ Caspase-3/7 Green Ready Flow™ Reagent (Invitrogen R37167) according to the manufacturer's instruction.

Mouse leukocyte adoptive transfer

Donor cells were collected from bone marrow (flushed with PBS) and spleen (smashing through a 70 μm cell strainer) from donor mice and lysed with RBC lysis buffer (420302 Biolegend). Cells were labeled with CellTracker™ Deep Red Dye (0.5μM in PBS, 37°C 15min), and injected i.v. (10^7 bone marrow cells and 10^7 splenocytes). Unless specified, tissues were harvested after 2h of cell injection. For egress assays, a total of 10^6 cells (50% of bone marrow cells and 50% of splenocytes) in 10μl PBS were injected intratumorally. Tissues were harvested 24h after the injection.

EdU assay

EdU (1 mg per mouse, Click-iT™ Plus EdU Alexa Fluor™ 594 Flow Cytometry Assay Kit, Invitrogen, C10646) was injected intraperitoneally into mice 4h before tissue collection. Tumor tissue was collected and digested as described above. Cells were first stained with viability dye (eBioscience™ Fixable Viability Dye eFluor™ 780, 65-0865-18), followed by surface staining as previous described. Then cells were fixed, permeabilized, and EdU detected according to the manufacturer's instruction.

CD8 T cell sorting and RNA extraction

To obtain $CD8^+$ T cells, tumor tissues were digested and processed as described above. Tumor-infiltrating leukocytes were then stained using anti-mouse CD45 (clone 30-F11 BUV 395), CD3e (clone KT3.1.1, BV421), CD4 (clone GK1.5 BV650), CD8a (clone 53-6.7 BV605), CD19 (clone 1D3, BB700), and NK1.1 (clone PK136, PE/Cy5) together with DRAQ7, and $CD45^+CD3^+CD8^+CD19^-$ cells were sorted using a BD Aria II. Flow cytometry sorted $CD8^+$ T cells were collected in RNAprotect Cell Reagent (cat. #76526, Qiagen). RNA was isolated using an RNeasy Plus Micro Kit (cat. #74034, Qiagen) according to the manufacturer's instructions. RNA integrity and quantity were assessed with a Bioanalyzer (Agilent Technologies) or a Nanodrop 2000 (ThermoFisher).

RNA extraction, reverse transcription and qPCR

Cells were collected and lysed using Trizol Reagent. RNA quantity and quality was analyzed using a Nanodrop 2000 (ThermoFisher) or Bioanalyzer. Reverse transcription was performed using PrimeScript™ RT Reagent Kit (Takara) according to the provided instructions. Q-PCR analyses were performed using PowerUp SYBR Green (Applied Biosystems). Quantification of the transcript was performed using the $2^{-\Delta\Delta Ct}$ method using *Rplp0 or Rpl32* as internal reference genes.

In vivo antibody treatments

To block LFA-1, anti-CD11a (clone M17/4, 100μg) and anti-CD18 (clone M18/2, 200 μg) antibodies were administered intravenously (i.v.). Anti-PD-1 antibody (anti-mouse PD-1, clone 29F.1A12™, 200μg) was administrated intraperitoneally (i.p) at day 4 or 6 (B16-F10-OVA) or day 6 or 7 (MC-38) after tumor engraftment. To deplete $CD8^+$ T cells, depletion antibody (anti-mouse CD8a, clone YTS 169.4, 100μg) was injected i.p. at the same day of PD-1 administration and repeated every 2 days. Isotype control rat IgG2a (clone 2A3) and rat IgG2b (clone LTF-2) antibodies were used. All antibodies were purchased from BioXCell.

Human CAR T cell generation

Human peripheral blood mononuclear cells (PBMCs) were collected from healthy donors' buffy coat (provided by University Hospitals of Geneva (HUG), Switzerland) using Ficoll-Paque Plus (Cytiva), then frozen in aliquots and stored in liquid nitrogen. Cryopreserved PBMCs were thawed and resuspended at $1x10^6$ cells per ml, activated for 3 days with Dynabeads human T-Activator CD3/CD28 (Gibco, 11132D) in the presence of recombinant human IL-2 (50 U/mL, PeproTech, 200-02) in RPMI1640 (Gibco) media supplemented with 10% heat-inactivated FBS (Gibco) and 1% penicillin-streptomycin at 37°C with 5% CO2. Activated T cells were transduced by culturing them for 48 hours in retronectin (Takara, T100B)-coated 24-well plates with retrovirus encoding second generation anti-CD19-CD28-CD3ζ CAR. The CAR construct was kindly provided by Dr. Crystal Mackall (Stanford University). Dynabeads were removed, and after washing, cells were cultured in complete media with 100 U/mL IL-2. At day 14, cells were harvested and frozen until further use. Transduction efficacy of CAR expression on T cells was evaluated by APC-conjugated streptavidin (Biolegend, 405207) binding to biotinylated protein L (ThermoFisher, 29997). Before use, CAR T cells were thawed, washed and rested for 4 hours at 37°C.

Human CAR T cell adoptive transfer

Human DoHH2 lymphoma cells were engrafted as described above. For long-term treatment experiments, $1x10^6$ CAR T cells or equal number of untransduced cells were injected i.v. into tumor-bearing mice at ZT1 or ZT13 on day 12 after tumor engraftment. For short-term homing experiment, $1x10^6$ CAR T cells were injected i.v. at ZT1 or ZT13 on day 15 after tumor engraftment. Twenty-four hours post transfer, tumors were harvested and digested using digestion medium (RPMI containing 1mg/mL collagenase IV (Worthington Biochemical Corporation), 2mg/mL collagenase D (Roche, 11088866001), 40 μg/mL DNase I (Roche 04716728001) and 2% heat-inactivated FCS) and incubated for 30 minutes at 37 °C. Single cell suspension were analyzed as described above.

Immunofluorescence imaging

Tumor tissues were collected and embedded into OCT blocks (CellPath) and kept at -80°C. Tumors were sectioned into 10 μm sections using a Cryostat. Sections were postfixed with 4% PFA for 10 min at room temperature. Following three washes with PBS, they were incubated with BlockAid™ Blocking Solution (Invitrogen™, B10710) for 2 h at RT. After PBS, sections were stained with an antibody diluted in Blocking Solution at 4°C overnight. The following antibodies were used, AF594 anti-mouse CD31 (clone MEC13.3, Biolegend 102520), FITC anti-mouse CD4 (clone, GK1.5, Biolegend 100405), AF647 anti-mouse CD54 (clone, YN1/1.7.4, Biolegend 116114), AF647 anti-mouse CD8 (clone 53-6.7, Biolegend 100724), AF488 anti mouse VCAM-1 (clone 429, Biolegend 105710), E-selectin (clone UZ6, Invitrogen MA1-06506), Goat anti-Rat IgG (H+L) Cross-Adsorbed Secondary Antibody, Alexa Fluor™ 647 (Invitrogen A21247). Slides were washed 3 times using PBS and stained with DAPI (300nM, Biolegend 422801) for 5 min at room temperature. Images were obtained as sections using a Zeiss Axio Examiner.Z1 confocal spinning disk microscope equipped with 405-, 488-, 561- and 640-nm laser sources. All image analyses were performed in ImageJ and Slidebook (Intelligent Imaging Innovations, 3i).

Human immunohistochemistry

Formalin-fixed, paraffin-embedded (FFPE) sections of melanoma were stained by immunohistochemistry using anti-CD4 (EP204) or anti-CD8 (SP16) (Zhongshan Golden Bridge Biotechnology, Beijing, China) primary antibodies. All staining was performed on the Leica Bond III automated platform (Leica Biosystems, Newcastle, UK) using Bond Polymer Refine Red Detection kit (DS9390). Slides were scanned with a Pannoramic P250 FLASH slide scanner (3DHistech, Budapest, Hungary).

Single cell sequencing and analysis

Tumors were harvested at different times of the day and processed as described above. Tumor infiltrating leukocytes were sorted ($CD45^+$ $DRAQ7^-$) using a Biorad S3 sorter in PBS with 1% BSA. Cellular suspension was loaded on a 10× Genomics Chromium instrument. Single-cell RNA-Seq libraries were prepared using Chromium Single Cell 3′ v3.1 Reagent Kit with dual indexes according to manufacturer's protocol. Library quantification and quality assessment was performed using a Qubit fluorometer (ThermoFisher Scientific) and a Tapestation (DNA High sensitivity chip - Agilent Technologies). Libraries were sequenced on an Illumina NovaSeq 6000 using paired-end 28 × 90 bp as sequencing mode. In total, 30693 single cells were sequenced (ZT1: 9764; ZT7: 7933; ZT13: 6255; ZT19: 6651).

Raw count matrices were generated with Cell Ranger v6.1.2 with mouse genome build mm10 as reference. Genes expressed in less than 20 cells were removed. Cells expressing less than 200 features, more than 7500 features, or more than 10% of mitochondrial genes were removed from further analysis. Dimensionality reduction and clustering analysis were done using Seurat v4.[56] Cells were annotated by conventional cell markers: B (*Cd79a, Igkc*), cDC1 (*Clec9a, Xcr1*), cDC2 (*H2-Aa, H2-Ab1, Itgax, Clec10a*), activated cDC (*Ccr7, Fscn1*), pDC (*Siglech, Bst2*), macrophage (*Cd68, Itgam*), monocyte (*Ly6c2, Ccr2*), neutrophil (*G0s2, Csf3r*), NK (*Nkg7, Klrb1c*), γδT (*Trdc, Tcrg-C1*), dendritic epidermal T cells (*Trdv4, Tcrg-C1*), CD4 (*Trac, Cd4*), CD8 (*Trac, Cd8a*), Treg (*Foxp3, Ctla4*), melanocyte (*Mlana, Dct*), and mitotic cells (*Birc5, Top2a*). 'Anti-tumorigenic lymphocytes' include NK, γδT, NKT, CD8 effector, CD4 naïve, CD8 effector memory, CD8 mitotic, and CD4 effector clusters, whereas 'Pro-tumorigenic lymphocytes' include Treg, Treg mitotic and CD8 exhausted clusters. Further annotation of CD4 and CD8 T cell subclusters cells were based on exhaustion (*Tox, Lag3, Pdcd1, Havcr2*), effector (*Gzmb, Prf1, Ifng, Il2, Il4*), memory (*Gzmk, Itga4*), and memory/naïve (*Tcf7, Sell, Ccr7, Lef1*) markers. Oscillatory genes were identified by Discorhythm[58] with each cell as one read. Gene set over-representation analyses were performed with clusterProfiler[57] and gene signature scores were calculated by GSVA.[59] Survival analyses were performed by using the TCGAbiolinks package.[60] Cosinor fitting of gene expression was performed by using the cosinor package.

ZeitZeiger analysis

The ZeitZeiger[31] model was trained using mouse melanoma scRNAseq data from the present study, mouse skin scRNAseq data from in-house, mouse skin scRNAseq data from GSE223109,[47] and mouse skin bulk RNAseq data from GSE115104[48] and GSE83855[49] data sets. To balance the representation of scRNAseq vs RNAseq and melanoma vs healthy skin data, the melanoma scRNAseq dataset was randomly sampled by 60% four times and the in-house skin scRNAseq dataset was randomly sampled by 60% two times to form the training set. For scRNAseq datasets, pseudobulk expression in each mouse was calculated and multiplied by 100 to generate the transcript per million as in data for training ZeitZeiger. Each dataset was randomly divided into a training set and a testing set at a ratio of 6:4. Training data and testing data were batch effect corrected by combat from the sva package.[61] Conserved coefficients were summarized from 20 runs of cross validation with different random seeds and different sumabsv and nSpc parameters. The genes *Klf9, Nr1d1, Cry2, Per1, Gapdh, Ppia, and Psmb2* were manually added to the coefficients, as previously described.[63] Further validation of the trained ZeitZeiger model was performed using RNAseq or RMA-normalized microarray data from both mouse (GSE114943,[48] GSE174155,[50] GSE38622,[51] GSE38623[51]) and human (GSE35635,[52] GSE205155,[53] GSE112660[54] and GSE139305[55]). To correct for the diurnal and nocturnal behavioral difference between human and mouse, predicted human sampling time were generated by adding 12h.

Estimation of cell composition in TCGA melanoma patients

To estimate the ratio of exhausted vs non-exhausted $CD8^+$ T cells, as well as major immune subsets, cells from GSE120575[33] were annotated as described earlier and the top 20 differentially expressed genes were used to estimate the immune cell composition by cibersortx .[64]

QUANTIFICATION AND STATISTICAL ANALYSIS

Unless specified, all data were plotted from independent biological replicates. Data was analyzed using Prism 9 and Prism 10 (GraphPad). $^*P < 0.05$; $^{**}P < 0.01$; $^{***}P < 0.001$; $^{****}P < 0.0001$.

CellPress
OPEN ACCESS

Supplemental figures

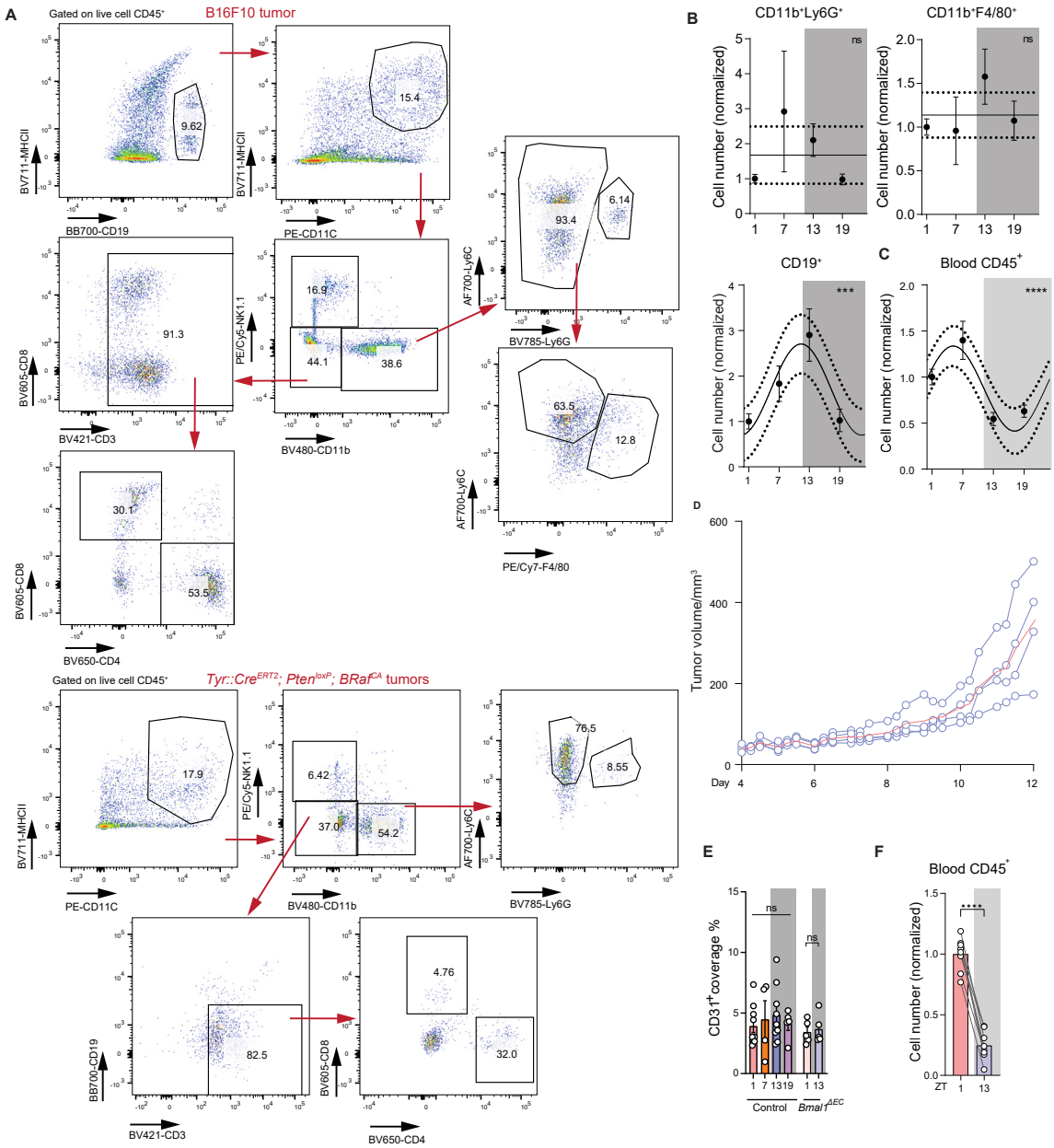

Figure S1. Time of day of harvest dictates numbers of tumor-infiltrating leukocytes, related to Figure 1

(A) Gating strategy of leukocytes in B16-F10-OVA and *Tyr::Cre^{ERT2}; Pten^{loxP}; BRaf^{CA}* tumors.

(B) Normalized total cell numbers of leukocyte subsets in B16-F10-OVA tumors, harvested at 4 different times of the day (zeitgeber time [ZT]); n = 15, 11, 11, 12 mice from 4 independent experiments, cosinor analysis.

(C) Blood leukocyte numbers sampled at 4 different times of the day from B16-F10-OVA tumor-bearing mice, n = 18, 14, 14, 10 mice from 5 independent experiments, cosinor analysis.

(D) Tumor volume of B16-F10-OVA tumors, measured 3 times a day, n = 4 mice.

(E) Quantification of the CD31$^+$ area in B16-F10-OVA tumors, harvested at ZT1 or ZT13, n = 10, 4, 9, 5, 5, 5 mice, one-way ANOVA, and unpaired Student's t test.

(F) Normalized numbers of blood leukocyte sampled at ZT1 or ZT13 from *Tyr::Cre^{ERT2}; Pten^{loxP}; BRaf^{CA}* tumor-bearing mice, n = 8 mice from 2 independent experiments, paired Student's t test. All data are represented as mean ± SEM, ns, not significant. ***p < 0.001; ****p < 0.0001.

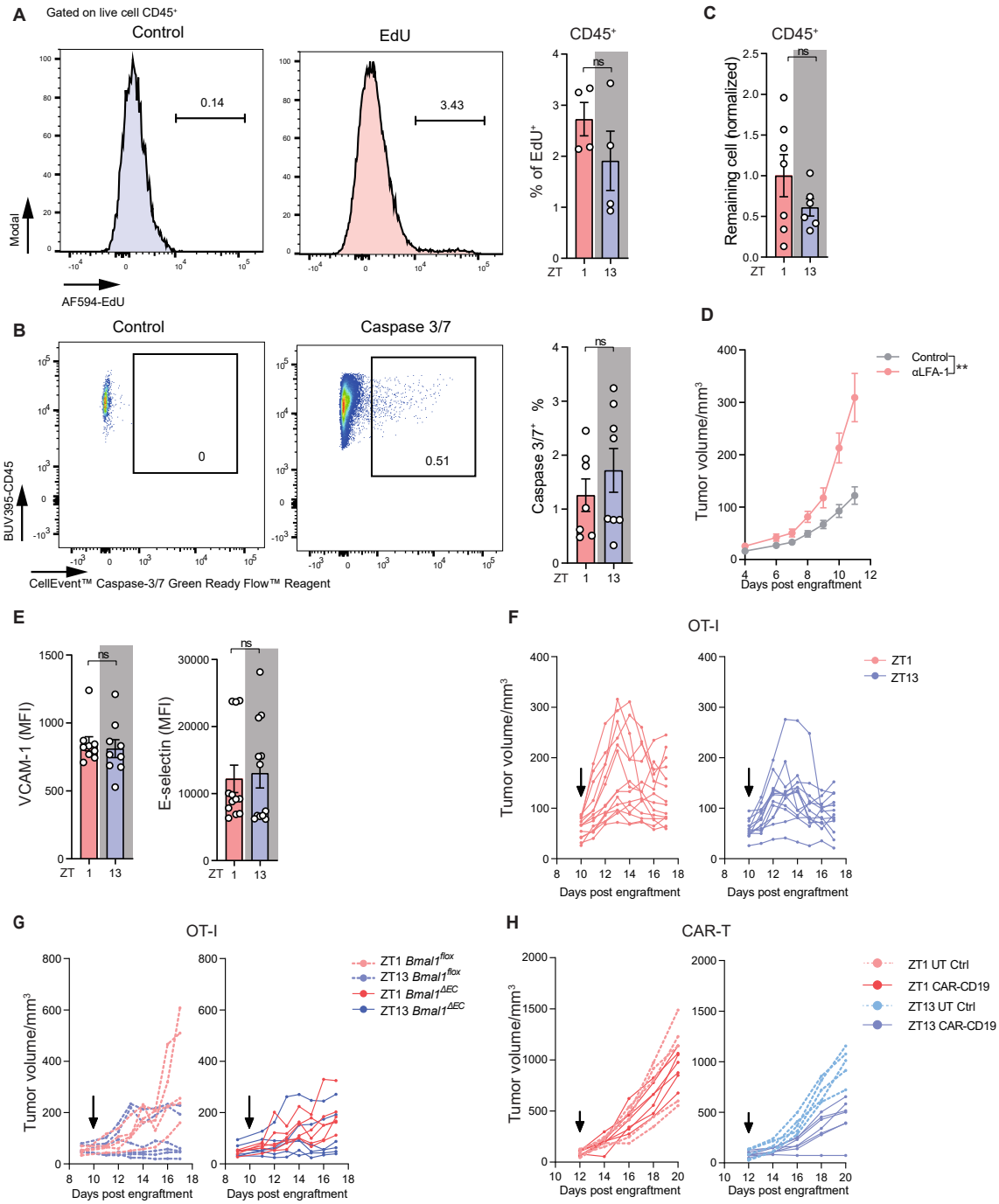

Figure S2. Circadian leukocyte infiltration and T cell therapy, related to Figure 2

(A) Gating strategy and quantification of EdU$^+$ leukocytes in B16-F10-OVA tumors, n = 4 mice, unpaired Student's t test.

(B) Gating strategy and quantification of caspase-3/-7$^+$ leukocytes in B16-F10-OVA tumors, harvested at ZT1 (n = 7 mice) or ZT13 (n = 8 mice), from 2 independent experiments, unpaired Student's t test.

(C) Normalized numbers of remaining cells in tumors 24 h post intratumoral injection of 10^6 leukocytes at ZT1 (n = 7 mice) or ZT13 (n = 6 mice), from 2 independent experiments, unpaired Student's t test.

(D) Tumor volume after anti-LFA-1 treatment (n = 8 mice), isotype control (n = 11 mice), from 2 independent experiments, two-way ANOVA.

(E) Quantification of VCAM-1 (n = 9 sections from 3 mice) or E-selectin (n = 12 sections from 4 mice) expression on CD31$^+$ cells in B16-F10-OVA tumors, harvested at ZT1 or ZT13, from 2 independent experiments, unpaired Student's t test. All data are represented as mean ± SEM, ns, not significant.

(F) Tumor volume after i.v. injection of 10^6 activated OT-I cells at ZT1 (n = 14 mice) or ZT13 (n = 13 mice), from 3 independent experiments.

(legend continued on next page)

(G) Tumor volume after i.v. injection of 10^6 activated OT-I cells at ZT1 (*Bmal1*^{flox} n = 5 mice, *Bmal1*$^{\Delta EC}$ n = 6 mice) or ZT13 (n = 6 mice), from 2 independent experiments.

(H) Tumor volume after i.v. injection of 10^6 anti-human CD19 CAR-CD28-CD3ζ T cells in DoHH2 tumor-bearing NSG mice at ZT1 (UT, untransduced T cells, n = 5 mice, CAR T, n = 7 mice) or ZT13 (UT, n = 5 mice, CAR T, n = 7 mice), from 2 independent experiments. All data are represented as mean ± SEM, ns, not significant. $^{**}p < 0.01$.

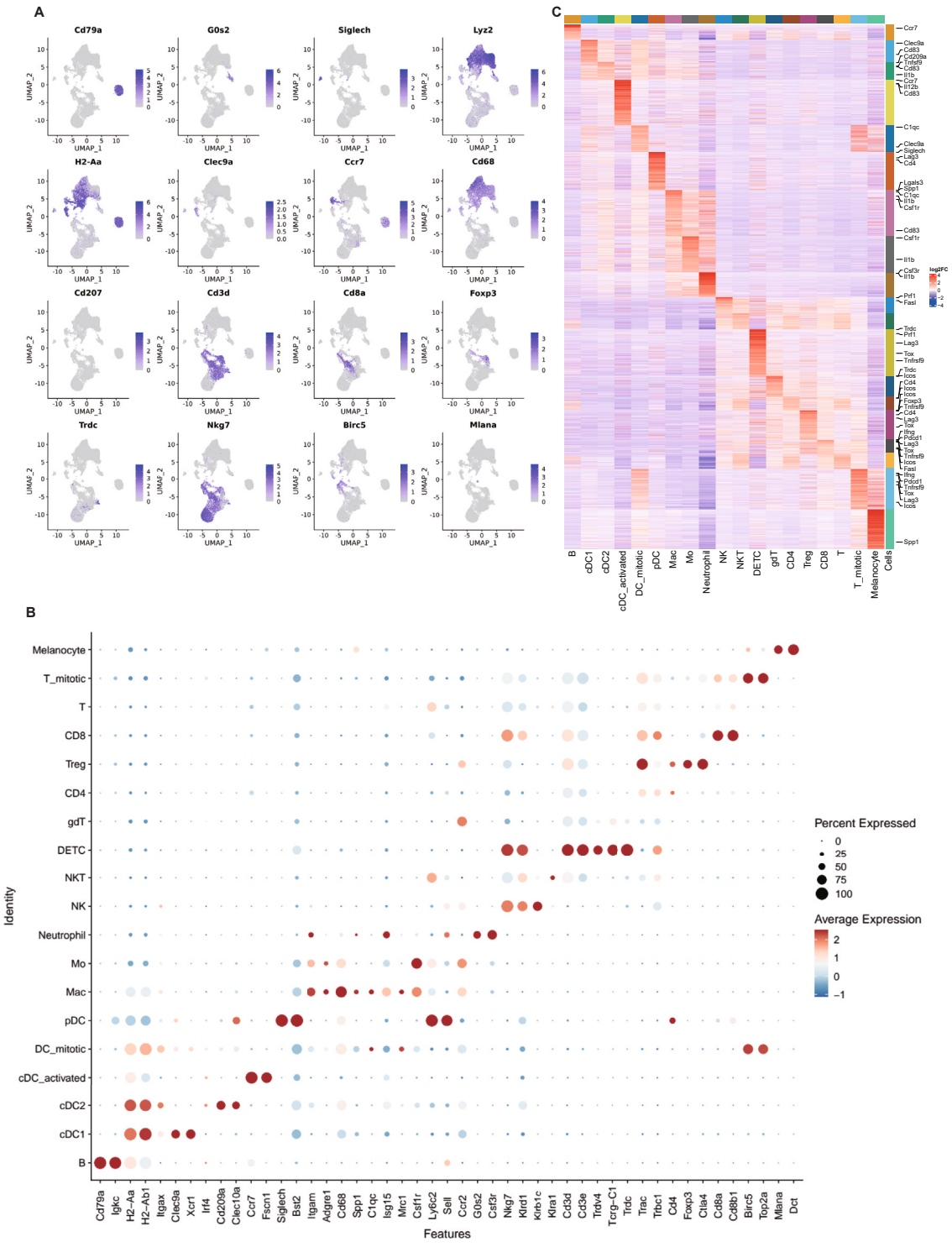

Figure S3. Identification of TIL subsets, related to Figure 3

(A–C) Feature plot and heatmap of genes to identify each leukocyte cluster obtained by scRNA-seq of B16-F10-OVA tumors, harvested at 4 different times of the day.

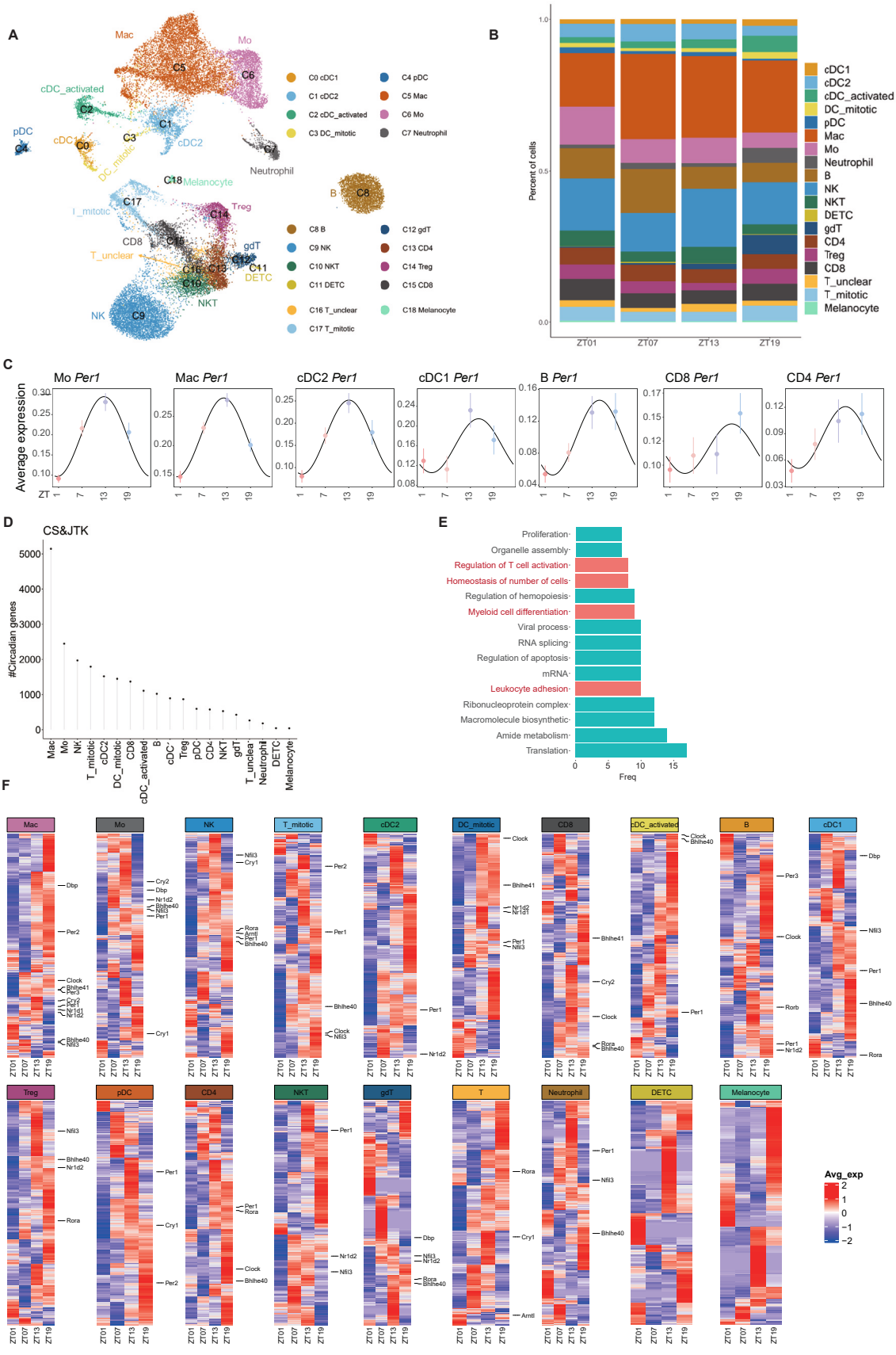

(legend on next page)

Figure S4. Diurnal oscillating TILs, related to Figure 3

(A) UMAP representation of scRNA-seq analyses of TILs harvested at 4 different times of the day.

(B) Relative abundance of immune cells per cluster across different times of the day.

(C) Expression of the circadian gene *Per1* in each leukocyte cluster obtained by scRNA-seq of B16-F10-OVA tumors, harvested at 4 different times of the day.

(D) Number of significantly oscillating genes detected in each cluster using cosinor (CS) and JTK cycle analyses.

(E) Top oscillatory Gene Ontology pathways common in the different immune cell clusters.

(F) Heatmap of oscillating genes of each cluster. Circadian genes are highlighted.

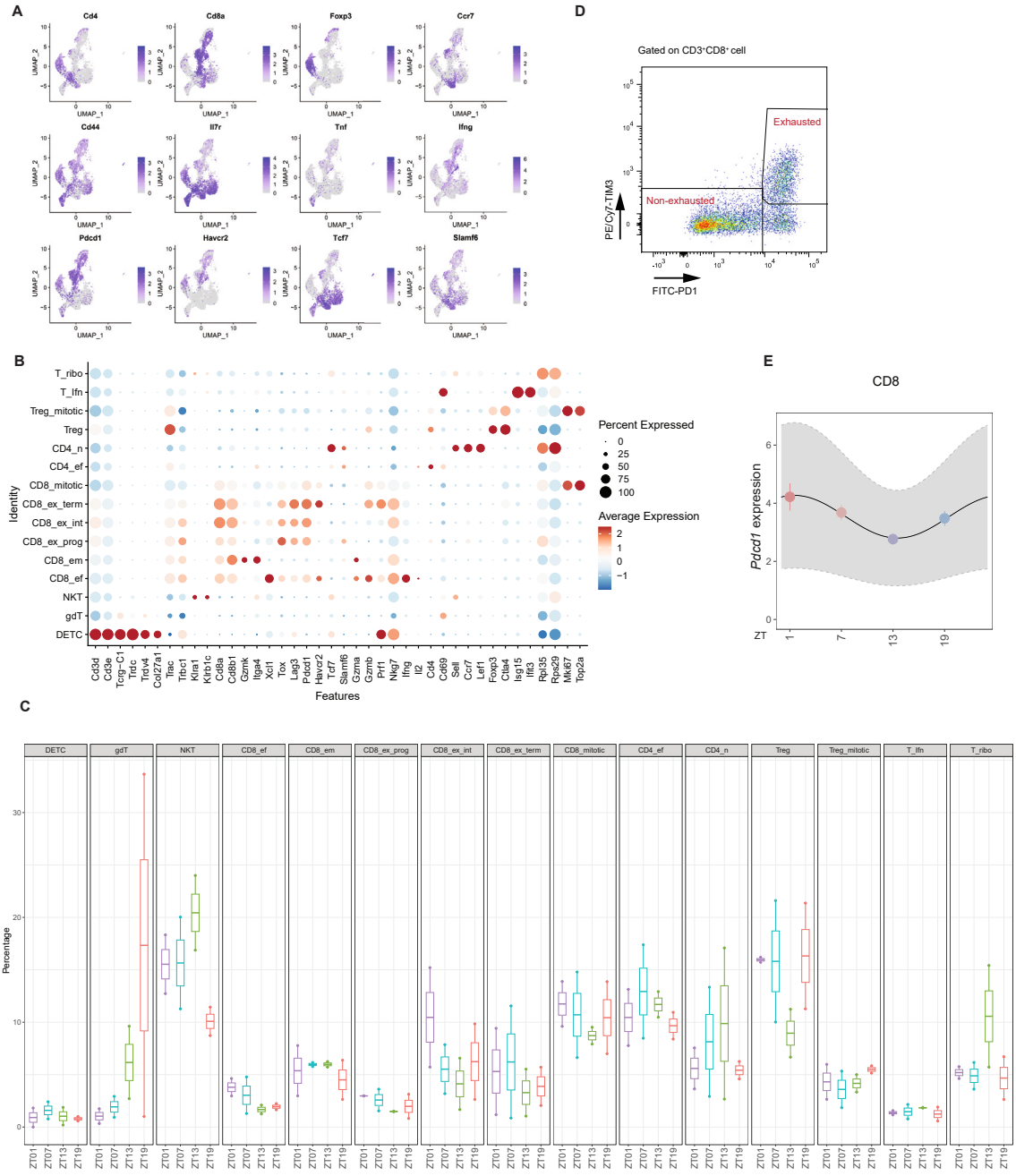

Figure S5. Diurnal oscillating genes in TILs, related to Figure 3

(A and B) Feature plot and dot plot of genes to identify different T cell clusters obtained by scRNA-seq of B16-F10-OVA tumors, harvested at 4 different times of the day.

(C) Relative abundance of each T cell cluster across different times of the day.

(D) Gating strategy of exhausted and non-exhausted $CD8^+$ T cells, pre-gated on CD8 T cells.

(E) Expression of *Pdcd1* quantified by pseudobulk analysis of the $CD8^+$ cluster obtained by scRNA-seq of B16-F10-OVA tumors, harvested at 4 different times of the day. To reduce the sparseness of scRNA-seq data, $CD8^+$ cluster was randomly sampled by 20% for 10 times with different seeds. The expression levels of *Pdcd1* at 4 different times of the day were averaged within each pseudobulk cell.

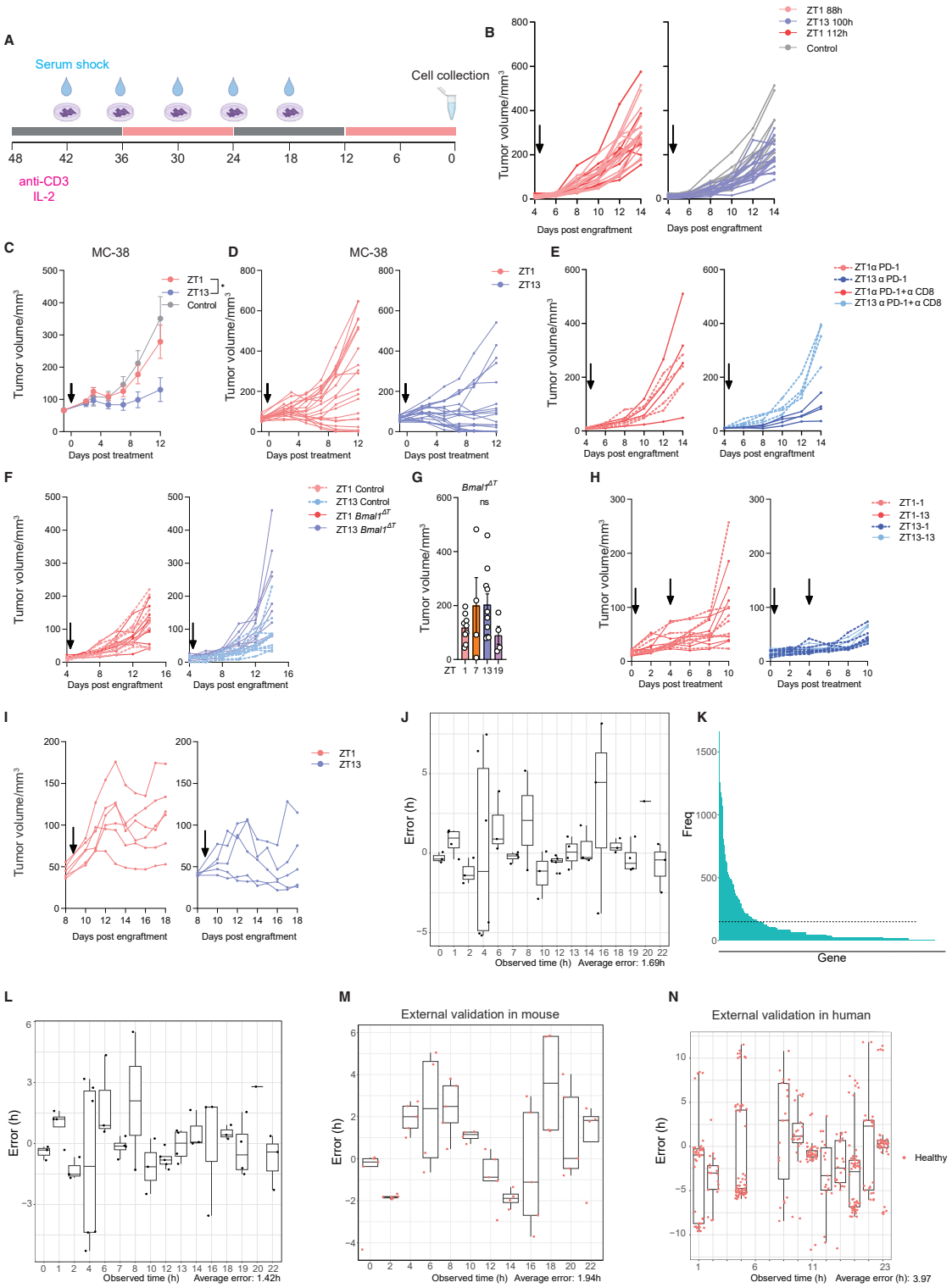

Figure S6. CD8⁺ T cell phenotype oscillates in mice and humans, related to Figures 4, 5, and 6

(A) Schematic overview of T cell synchronization *in vitro*.

(B) Tumor volume after anti-PD-1 treatment administered at ZT1 or ZT13 in B16-F10-OVA tumors; *n* = 15, 15, 9 mice; control *n* = 11 mice, from 3 independent experiments.

(legend continued on next page)

(C and D) Tumor volume after anti-PD-1 treatment administered at ZT1 or ZT13 in MC-38 tumors; n = 20 mice; control n = 10 mice, from 2 independent experiments, two-way ANOVA.
(E) Tumor volume after anti-PD-1 treatment administered at ZT1 or ZT13 in B16-F10-OVA tumors with or without CD8 depletion, n = 4 mice.
(F) Tumor volume after anti-PD-1 treatment administered at ZT1 or ZT13 in B16-F10-OVA tumors in control (ZT1, n = 9 mice; ZT13, n = 10 mice) or *Bmal1*$^{\Delta T}$ (ZT1, n = 9 mice; ZT13, n = 10 mice), from 3 independent experiments.
(G) Tumor volume at 14 days post B16-F10-OVA tumor engraftment in *Bmal1*$^{\Delta T}$ mice, after anti-PD-1 treatment at 4 different times of the day (n = 9, 4, 10, 4 mice), from 3 independent experiments, one-way ANOVA; data are represented as mean ± SEM.
(H) Tumor volume after two doses of anti-PD-1 treatment administered at ZT1 or ZT13; n = 7 mice, from 2 independent experiments.
(I) Tumor volume after combination therapy of anti-PD-1 and OT-I cells administered at ZT1 (n = 6 mice) or ZT13 (n = 5 mice), from 2 independent experiments.
(J) Error (in h) of the time-predicting algorithm in mouse using full gene lists as internal validation gene sets, n = 54 mice; data are represented as median and quartile.
(K) Frequency of ZeitZeiger coefficient genes across 20 runs; the dashed line indicates the cut-off for 57 conserved coefficient genes.
(L) Error (in h) of the time-predicting algorithm in mouse using 57 conserved coefficient genes in internal validation gene sets, n = 54 mice; data are represented as median and quartile.
(M) Error distribution of Figure 6E, external validation in mouse, n = 56 mice; data are represented as median and quartile.
(N) Error distribution of Figure 6F, external validation in healthy human patients, n = 369 patients; data are represented as median and quartile, $^{*}p < 0.05$.